JGR Solid Earth

RESEARCH ARTICLE
10.1029/2018JB016582

Lateral and Vertical Heterogeneity in the Lithospheric Mantle at the Northern Margin of the Pannonian Basin Reconstructed From Peridotite Xenolith Microstructures

N. Liptai[1,2,3], K. Hidas[4,5], A. Tommasi[6], L. Patkó[1], I. J. Kovács[7,8], W. L. Griffin[2], S. Y. O'Reilly[2], N. J. Pearson[2], and C. Szabó[1]

[1]Lithosphere Fluid Research Lab, Institute of Geography and Earth Sciences, Eötvös University, Budapest, Hungary, [2]Australian Research Council Centre of Excellence for Core to Crust Fluid Systems and GEMOC, Department of Earth and Planetary Sciences, Macquarie University, North Ryde, New South Wales, Australia, [3]Now at MTA CSFK Lendület Pannon LitH$_2$Oscope Research Group, MTA Research Centre for Astronomy and Earth Sciences, Sopron, Hungary, [4]Instituto Andaluz de Ciencias de la Tierra, CSIC and UGR, Armilla, Spain, [5]Departamento de Geodinámica, Universidad de Granada, Granada, Spain, [6]Géosciences Montpellier, Université de Montpellier and CNRS, CC 60, Montpellier, cedex 5, France, [7]Geodetic and Geophysical Institute, MTA Research Centre for Astronomy and Earth Sciences, Sopron, Hungary, [8]MTA CSFK Lendület Pannon LitH$_2$Oscope Research Group, MTA Research Centre for Astronomy and Earth Sciences, Sopron, Hungary

Key Points:
- Variable microstructures of peridotite xenoliths from the Nógrád-Gömör Volcanic Field indicate heterogeneous deformation and subsequent annealing
- Olivine crystal preferred orientations suggest deformation in a transpressional regime, associated with the recent tectonic evolution of the region
- Postkinematic annealing is linked to the presence of percolating metasomatic melts in the lithospheric mantle

Supporting Information:
- Supporting Information S1

Correspondence to:
C. Szabó,
cszabo@elte.hu

Citation:
Liptai, N., Hidas, K., Tommasi, A., Patkó, L., Kovács, I. J., Griffin, W. L., et al. (2019). Lateral and vertical heterogeneity in the lithospheric mantle at the northern margin of the Pannonian Basin reconstructed from peridotite xenolith microstructures. *Journal of Geophysical Research: Solid Earth*, *124*, 6315–6336. https://doi.org/10.1029/2018JB016582

Received 21 AUG 2018
Accepted 21 MAY 2019
Accepted article online 29 MAY 2019
Published online 2 JUL 2019

Abstract This study analyzes the microstructures and deformational characteristics of spinel peridotite xenoliths from the Nógrád-Gömör Volcanic Field (NGVF), located on the northern margin of a young extensional basin presently affected by compression. The xenoliths show a wide range of microstructures, bearing the imprints of heterogeneous deformation and variable degrees of subsequent annealing. Olivine crystal preferred orientations (CPOs) have dominantly [010]-fiber and orthorhombic patterns. Orthopyroxene CPOs indicate coeval deformation with olivine. Olivine J indices correlate positively with equilibration temperatures, suggesting that the CPO strength increases with depth. In contrast, the intensity of intragranular deformation in olivine varies as a function of the sampling locality. We interpret the microstructures and CPO patterns as recording deformation by dislocation creep in a transpressional regime, which is consistent with recent tectonic evolution in the Carpathian-Pannonian region due to the convergence between the Adria microplate and the European platform. Postkinematic annealing is probably linked to percolation of metasomatism by mafic melts through the upper mantle of the NGVF prior to the eruption of the host alkali basalt. Elevated equilibration temperatures in xenoliths from the central part of the volcanic field are interpreted to be associated with the last metasomatic event, which only shortly preceded the ascent of the host magma. Despite well-developed olivine CPOs in the xenoliths, which imply a strong seismic anisotropy, the lithospheric mantle alone cannot account for the shear wave splitting delay times measured in the NGVF, indicating that deformation in both the lithosphere and the asthenosphere contributes to the observed shear wave splitting.

1. Introduction

The subcontinental lithospheric mantle (SCLM) represents a chemical, thermal, and mechanical boundary layer that physically isolates the overlying continental crust from the more dynamic interior of the Earth (e.g., Griffin et al., 1999, 2009, and references therein). Chemical and physical heterogeneities fundamentally influence the mechanical response of the SCLM to tectonic forces (e.g., Tommasi & Vauchez, 2015). However, the origin and extent of these heterogeneities are still poorly constrained. For better understanding these processes, mantle xenoliths from tectonically active regions are of paramount interest as they can provide information on both the deformation history and seismic properties of the lithospheric mantle. However, the reconstruction of deformation processes is often complicated by synkinematic/postkinematic metasomatism (e.g., Higgie & Tommasi, 2012; Kourim et al., 2015; Soustelle et al., 2013), hydration (e.g., Demouchy et al., 2012; Jung & Karato, 2001; Soustelle et al., 2010), and annealing (e.g., Tommasi et al., 2008; Vauchez et al., 2005; Zaffarana et al., 2014).

The Carpathian-Pannonian region (CPR) is a Cenozoic Mediterranean-style extensional back-arc basin, which offers a unique opportunity to study the composition of the SCLM at various stages of lithospheric thinning and subsequent tectonic inversion. Neogene alkali basalts transported large amounts of mantle xenoliths to the surface throughout the basin system (see Szabó et al., 2004, for a review). Deformation studies of mantle xenoliths from both the marginal areas and the central part of the Pannonian Basin have revealed a dependence of microstructures and crystal preferred orientation (CPO) types on equilibration temperatures, which probably record different depths of origin (e.g., Aradi et al., 2017; Falus et al., 2008, 2011; Hidas et al., 2007; Kovács et al., 2012; Kovács, Patkó, et al., 2018). The Nógrád-Gömör Volcanic Field (NGVF) is situated at the transition between the marginal and central regions of the thinned CPR lithosphere. Mantle xenoliths from this locality record a complex metasomatic history (Liptai et al., 2017). However, despite the well-documented geochemical background, the relationship between mantle metasomatism and deformation beneath the NGVF has not been analyzed in detail yet, as there is only limited data available on the latter (Klébesz et al., 2015; Liptai et al., 2013). In this study, we present petro-structural data (microstructures and CPOs of the major rock forming minerals) for the xenolith set previously studied from a petrological and geochemical point of view by Liptai et al. (2017). Based on these data, we reconstruct the deformation and annealing history, calculate the seismic anisotropy of the xenoliths, and compare them with seismological data of the broader region, aiming to constrain the evolution of the lithospheric mantle in the northern part of the Pannonian Basin.

2. Geological Setting

The CPR is a young extensional basin system, surrounded by the Alps, the Carpathians, and the Dinarides (Figure 1a). It is composed of two microplates, ALCAPA (northwest) and Tisza-Dacia (southeast), separated by the Mid-Hungarian Fault Zone (Csontos, 1995). The tectonic evolution of the CPR started in the Palaeogene, with the eastward extrusion of the ALCAPA microplate from the Alpine collision zone (Kázmér & Kovács, 1985), which juxtaposed the two microplates. There is no consensus as to whether this extrusion involved only the crust (e.g., Horváth et al., 2006, 2014) or the lithospheric mantle as well (e.g., Kovács et al., 2012; Kovács & Szabó, 2008). It was followed by opposite rotation of the two microplates during the late Oligocene to early Miocene (Csontos et al., 1992; Márton, 1987). In the middle Miocene (17–14 Ma), the CPR was submitted to a major extensional phase, with intense thinning accompanied by thermal erosion of the lithosphere and asthenospheric uplift (Csontos, 1995; Horváth, 1993; Stegena et al., 1975). Both the extrusion and the Miocene extension were accompanied by asthenospheric flow (Horváth & Faccenna, 2011; Kovács et al., 2012) linked to rollback of the oceanic plate that was subducting under the Eastern Carpathians (e.g., Fodor et al., 1999; Horváth et al., 2006). Finally, the collision of ALCAPA and Tisza-Dacia with the stable European platform gradually led to a compressive phase since the late Miocene (Bada et al., 2007; Horváth and Cloetingh, 1996; Horváth et al., 2006).

Widespread volcanic activity, including rhyolitic, intermediate calc-alkaline, alkali basaltic, and ultrapotassic magmas, started in the Miocene and continued until the Pleistocene (Harangi & Lenkey, 2007; Kovács & Szabó, 2008; Seghedi & Downes, 2011; Szabó et al., 1992). The Miocene-Pleistocene alkali basalts (Embey-Isztin et al., 1993; Pécskay et al., 1995, 2006) contain mantle xenoliths in five major volcanic fields, which are from west to east: Styrian Basin, Little Hungarian Plain, Bakony-Balaton Highland, Nógrád-Gömör, and Perşani Mountains (Figure 1a).

The NGVF consists of dominantly effusive and pyroclastic structures. Upper mantle xenoliths are found at eleven localities, from Podrečany in the northwest to Bárna in the southeast (Figure 1b). The xenolith-hosting part of the volcanic field can be divided into three areas based on their age and location. The northern and southern areas are characterized by isolated volcanic cones, whereas the central area is composed of two basalt plateaus (Babi Hill and Medves Plateau) with 3 xenolith occurrences each, and a monogenetic cone (Fil'akovo-Kerčik). K-Ar eruption ages are older (6.4–4.9 Ma) in the northern part than those of the Fil'akovo-Kerčik volcano (4.0 Ma) and the two basalt plateaus of the central part (3.0–2.5 Ma; Balogh et al., 1986). The youngest ages occur in the southern part (2.5 Ma). U/Pb and (U-Th)/He ages (Hurai et al., 2013) for the northern (7.0–5.9 Ma) and central part (3.0–1.7 Ma) are in good agreement with the earlier K-Ar data.

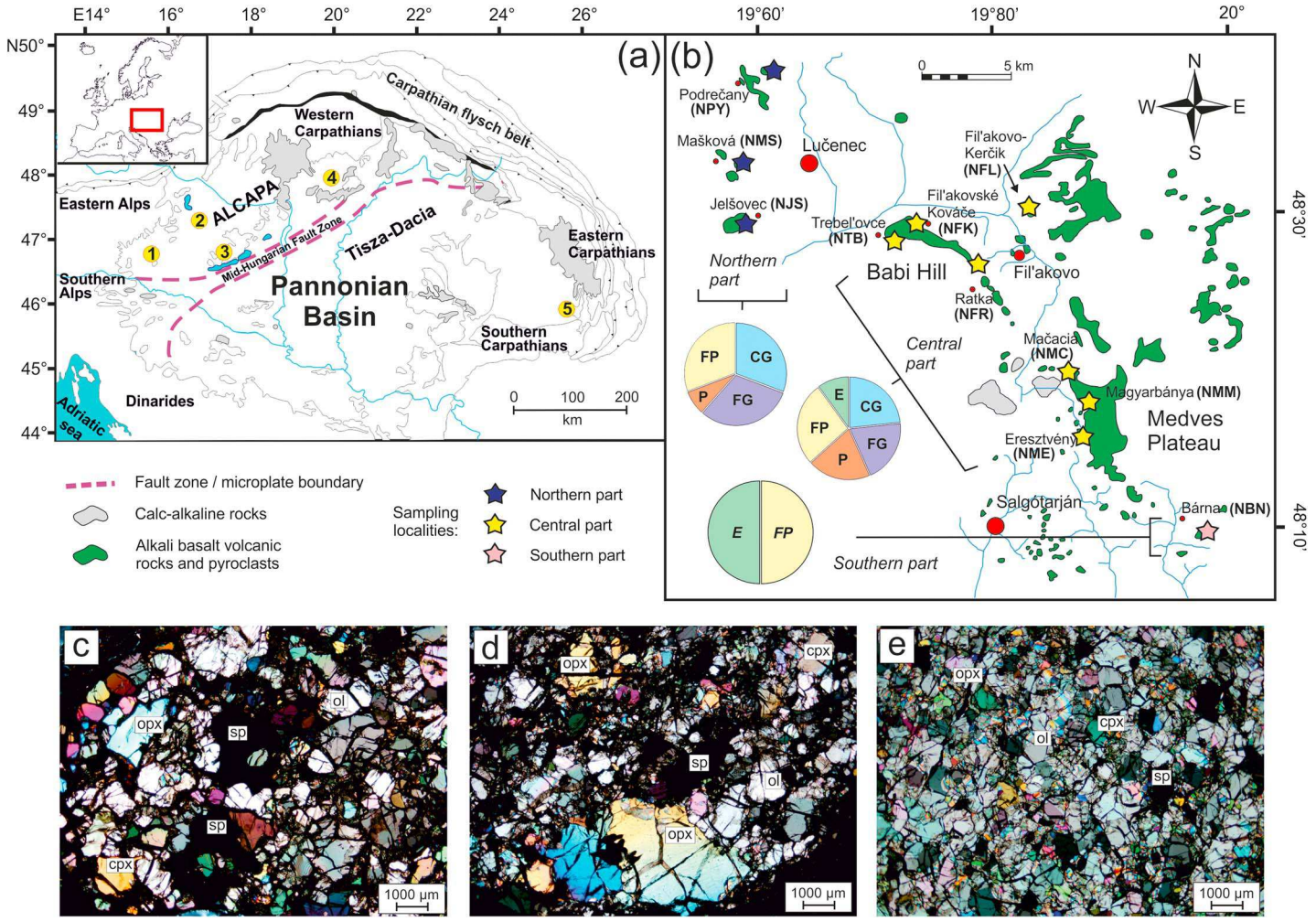

Figure 1. (a) Locations of the alkali basalt occurrences hosting ultramafic xenoliths in the Carpathian-Pannonian region. 1—Styrian Basin; 2—Little Hungarian Plain; 3—Bakony-Balaton Highland; 4—Nógrád-Gömör (NGVF); 5—Perşani Mountains. (b) Alkali basalt outcrops of the NGVF and sampling localities (with abbreviations) of the xenoliths presented in this study. Pie charts indicate the distribution of texture types in the northern, central, and southern parts of the volcanic field (see text for details). CG = coarse granular; FG = fine granular, porphyroclastic; Ffine porphyroclastic; E = equigranular. (c–e) Cross-polarized transmitted light photomicrographs of representative xenoliths with granular, porphyroclastic, and equigranular textures, respectively. NGVF = Nógrád-Gömör Volcanic Field.

3. Provenance and Geochemistry of the Nógrád-Gömör Xenoliths

Peridotite xenoliths from the NGVF display a wide range of textural and geochemical characteristics (Szabó & Taylor, 1994). More recently, a lherzolitic and a wehrlitic series were distinguished. Liptai et al. (2017) have analyzed the geochemistry of the lherzolitic suite and, based on the major and trace element contents, have reconstructed three metasomatic events. These include (1) formation of Nb-poor amphiboles, presumably due to interaction with a subduction-related volatile-rich melt, (2) reaction with a mafic melt of intraplate origin, resulting in the formation of Nb-rich amphiboles and enrichment of U-Th-Nb-Ta-light rare earth element (LREE) in clinopyroxenes, and (3) reaction with an intraplate melt of slightly different composition, resulting in enrichment of Fe and Mn in olivine and pyroxenes, Ti in spinel, and LREE in pyroxenes. The first of these events is likely older than the Miocene extension, as the last subduction in the vicinity of the NGVF is suggested to have occurred prior to the extrusion of the ALCAPA microplate (Kovács & Szabó, 2008). The latter two events involve melts that percolated the upper mantle of the NGVF after the extension. The last process is responsible for the formation of the wehrlitic xenolith suite in the central domain of the NGVF (Patkó et al., 2013).

Liptai et al. (2017) also reported equilibration temperatures for the xenoliths analyzed in the present study. They used several thermometers, including the two-pyroxene thermometer of Brey and Köhler (1990; $\sigma = 15$

°C), the Ca-in-opx thermometer of Brey and Köhler (1990) with corrections by Nimis and Grütter (2010; $\sigma =$ 36 °C), and the newly-developed two-pyroxene rare earth element (REE) thermometer of Liang et al. (2013; $\sigma =$ 1–59 °C; see Liptai et al., 2017; Table 1). Equilibration temperatures of NGVF xenoliths determined with the REE-based thermometer (901–1154 °C) are higher by 50–100 °C on average than those calculated with major element-based thermometers (845–1058 °C with the two-pyroxene method and 921–1044 °C with the Ca-in-opx method; see Figure 9 of Liptai et al., 2017). This discrepancy probably reflects the higher closure temperatures of REE exchange between orthopyroxene and clinopyroxene than of divalent major element cations (Van Orman et al., 2001). Such discrepancies are expected for abyssal peridotites, where the cooling rate is expected to be higher (e.g., Coogan et al., 2002), but not in the subcontinental upper mantle, which is assumed to equilibrate over long periods of time. Liptai et al. (2017) interpreted the difference in the REE and major element equilibration temperatures as a sign of recent and rapid cooling in the NGVF mantle, linked to postextensional thermal relaxation. If plotted onto the alkaline province geotherm of Jones et al. (1983), the equilibration temperatures determined using the major-element-based thermometers (Table 1) correspond to depths of ~35–50 km (Liptai et al., 2017). Equilibration temperatures in general are lower in the southern and northern parts (apart from a few outliers), whereas xenoliths from the central part show higher values (Table 1).

4. Analytical Methods

Electron backscatter diffraction (EBSD) measurements on Syton-polished thin sections were carried out at two different laboratories. Part of the samples were analyzed at the Geochemical Analysis Unit at CCFS-GEMOC, Macquarie University, on a Zeiss EVO MA15 scanning electron microscope equipped with an HKL NordlysNano EBSD detector, using AZtec analysis software (Oxford Instruments). Accelerating voltage was 20 kV and working distance was shifted between 12.5 and 25 mm. Another part was analyzed at Geosciences Montpellier (France) using a JEOL JSM-5600 SEM equipped with an Oxford HKL Technology EBSD system and Channel 5 software package, with 17 kV accelerating voltage and 25-mm working distance. Mapping usually covered most of the xenolith surface and the step size ranged between 20 and 70 μm depending on the grain size. Indexing rate varied between 55% and 92%, but in most samples it is >70%. Postacquisition data processing and calculation of deformation parameters presented in Table 1 are described in detail in the supporting information (Text S1). For samples with recognizable foliation/lineation structure, oriented thin sections were prepared in the structural reference frame plane *XZ*, which is parallel to the lineation and normal to the foliation. In the pole figures, lineation is oriented E-W and the pole of foliation, N-S. For straightforward comparison between samples, CPO data of randomly cut thin sections of samples in which the foliation could not be discriminated macroscopically were rotated so that the olivine CPO [100] and [010] maxima align in E-W and N-S directions in the pole figures, respectively. To characterize the olivine CPO strength and symmetry and intragranular misorientation, which results from stored dislocations, the J index, BA index, and grain orientation spread (GOS) were calculated using the free MTEX 4.5.2 Matlab toolbox (https://mtex-toolbox.github.io/; Bachmann et al., 2010; Hielscher & Schaeben, 2008; Mainprice et al., 2014; see Text S1 in the supporting information for more information).

Seismic properties at ambient conditions were calculated using modal proportions and CPO data of olivine, orthopyroxene and clinopyroxene, and elastic tensors for olivine, orthopyroxene, and clinopyroxene from Abramson et al. (1997), Jackson et al. (2007), and Isaak et al. (2006), respectively, using the ANISctfPC software (Mainprice, 1990) and applying a Voigt-Reuss-Hill averaging. Seismic properties of all xenoliths were averaged to obtain representative information for the subcontinental lithospheric mantle of the NGVF, considering that seismic waves average the seismic properties over large volumes around their paths. To do this averaging, we assumed that foliation and lineation of all samples have the same orientation. The calculated average seismic properties are therefore a maximum estimate for the seismic anisotropy of the NGVF lithospheric mantle.

5. Petrography and Microstructures

The geochemistry of the xenoliths has been described by Liptai et al. (2017). The xenoliths are spinel peridotites, with modal compositions ranging from harzburgite to wehrlite, but most are lherzolitic (Table 1).

Table 1
Summary of Petrography, Modal Compositions, Equilibration Temperatures, Olivine Textural Parameters, and Seismic Properties of the Studied NGVF Xenoliths

		Modal composition (%)					Equilibration temperatures (°C)			Calculated olivine parameters			Seismic properties			
													Vp (km/s)		AVp	AVs
Xenolith	Texture	Ol	Opx	Cpx	Sp	Amp	T_{BK}	T_{NG}	T_{REE}	J	BA	GOS	Maximum	Minimum	(%)	(%)
Northern part																
NMS1302A	Fine porph	84	12	4	<1		863	928	1021	4.6	0.22	3.2	8.74	7.83	11.0	7.55
NMS1304	Fine porph	78	13	8	<1	1	845	921	1030	2.8	0.66	2.2	8.65	8.03	7.4	5.19
NMS1305	Fine gr	59	25	14	2		918	942	1044	2.3	0.20	2.7	8.43	7.98	5.5	4.09
NMS1308	Porph	69	20	9	1	<1	926	930	980	2.6	0.29	3.0	8.53	7.97	6.8	5.22
NMS1310	Coarse gr	47	42	10	1		953	974	1027	3.7	0.33	2.6	8.35	8.01	4.1	4.17
NJS1302	Fine porph	73	15	10	2	<1	962	961	1063	2.1	0.26	2.2	8.53	7.94	7.1	4.31
NJS1304	Coarse gr	74	21	4	1		944	961	1052	3.5	0.45	2.6	8.62	7.89	8.8	5.81
NJS1306	Coarse gr	69	11	18	2		1025	1043	1145	4.8	0.23	2.2	8.50	7.91	7.3	4.68
NJS1307	Coarse gr	67	14	17	2		1024	1006	1097	4.3	0.26	3.2	8.56	7.91	7.9	5.50
NPY1301	Fine gr	66	18	13	2		941	952	999	3.0	0.27	2.9	8.55	7.93	7.6	4.85
NPY1310	Fine gr	55	15	27	3		936	967	1070	2.6	0.16	2.1	8.41	7.95	5.6	3.55
NPY1311	Fine porph	53	17	26	4		944	970	1052	2.4	0.19	2.3	8.42	7.92	6.1	4.06
NPY1314	Fine gr	56	23	19	2		928	958	1040	2.8	0.23	2.2	8.48	7.97	6.2	4.54
Central part																
NFL1302	Fine gr	78	7	13	2	<1	926	967	1031	2.6	0.27	2.0	8.59	7.96	7.6	5.76
NFL1305	Fine gr	54	29	16	1		940	971	1070	2.8	0.41	1.4	8.36	7.99	4.6	4.43
NFL1315A	Fine porph	90	7	3	<1	<1	901	969	991	3.8	0.46	1.8	8.84	7.92	11.0	7.99
NFL1316	Fine porph	75	19	6	<1		892	959	965	2.5	0.42	1.6	8.58	8.01	6.9	5.15
NFL1324	Porph	60	26	13	1	1.0	938	991	1030	4.3	0.36	2.4	8.56	7.87	8.4	5.47
NFL1326	Equi	80		18	1	1.5	N/A	N/A	N/A	3.1	0.49	1.5	8.70	7.98	8.7	5.43
NFL1327	Equi	88	<1	12	<1		952	1019	1112	3.0	0.34	1.5	8.72	7.95	9.3	6.07
NFL1329	Fine gr	69	14	15	1	<1	932	965	1013	2.4	0.28	1.3	8.54	7.96	7.0	5.28
NTB0306	Fine gr	78	12	10	<1		994	951	901	2.5	0.53	1.4	8.60	8.03	6.7	5.28
NTB0307	Fine porph	79	6	15	<1		1058	943	991	2.4	0.27	2.3	8.51	8.02	5.9	3.97
NTB1124	Coarse gr	76	10	11	3		993	1001	1031	6.0	0.39	1.3	8.69	7.97	8.6	6.08
NTB1116	Coarse gr	75	9	12	3		970	980	1015	4.4	0.62	1.6	8.76	7.95	9.8	6.48
NTB1122	Coarse gr	66	17	17	1		999	1044	1154	4.9	0.20	1.4	8.48	8.03	5.4	3.87
NFK0301	Porph	78	16	6	<1		996	984	1045	3.4	0.75	2.1	8.80	8.02	9.3	6.13
NFK1123	Fine gr	72	25	2	1		985	983	1022	4.0	0.45	1.4	8.70	8.06	7.7	5.81
NFK1108	Porph	87	5	8	<1		996	1044	1141	3.6	0.43	2.3	8.81	7.95	10.2	6.64
NFK1115	Equi	80	15	4	<1		913	972	1028	3.0	0.54	1.4	8.74	7.97	9.2	6.62
NFR1109	Coarse gr	81	11	6	1		1010	1022	1056	3.4	0.33	1.5	8.71	7.95	9.0	6.58
NFR0309	Fine porph	63	17	17	2		955	977	1047	2.4	0.21	1.9	8.46	7.96	6.0	4.32
NFR1107	Porph	74	16	9	1		952	985	1021	3.6	0.44	2.4	8.55	7.98	6.8	5.12
NMC1301	Coarse gr	75	11	14	<1		958	1000	1066	3.7	0.32	2.0	8.64	7.93	8.5	6.81
NMC1309	Coarse gr	72	7	20	1		942	990	1068	4.3	0.12	2.3	8.56	7.86	8.5	6.66
NMC1322	Fine porph	77	9	12	2		944	969	988	2.6	0.25	2.2	8.59	7.95	7.7	5.51
NMC1336A	Fine porph	57	24	16	3		961	980	1037	2.6	0.40	1.7	8.44	8.00	5.3	3.99
NMM1126	Porph	67	18	15	<1		974	983	990	6.1	0.60	2.1	8.69	7.93	9.2	6.85
NMM0318	Fine porph	61	16	22	1		951	983	1071	2.7	0.37	1.7	8.52	7.99	6.4	4.91
NMM1115	Fine porph	76	13	10	1		912	957	997	3.1	0.29	1.6	8.62	7.95	8.1	5.02
NME1122	Coarse gr	87	4	8	<1		968	968	958	4.3	0.34	2.0	8.69	7.97	8.7	6.49
NME0528	Porph	73	16	11	<1		947	984	1027	3.2	0.49	1.8	8.66	7.93	8.8	6.12
NME1116	Fine gr	64	19	16	1		947	984	1059	3.2	0.35	1.9	8.57	7.95	7.6	4.99
Southern part																
NBN0302A	Fine porph	88	5	5	1		902	932	1011	1.8	0.44	1.3	8.60	8.06	6.6	4.45
NBN0305	Equi	79	15	6	<1		912	933	1028	1.8	0.59	1.2	8.55	8.08	5.6	4.00
NBN0311	Fine porph	81	7	10	1		917	922	965	2.1	0.09	1.6	8.51	8.00	6.1	4.42
NBN0316	Equi	79	11	9	1		912	941	1122	1.7	0.67	1.3	8.52	8.15	4.5	3.18
NBN0319	Equi	70	16	13	1		888	941	1114	1.6	0.70	1.1	8.51	8.13	4.6	2.92
NBN0321	Fine porph	84	7	8	1		924	946	930	2.3	0.17	1.3	8.54	8.05	6.0	4.96

Abbreviations: gr—granular; porph—porphyroclastic; equi—equigranular; GOS—area-weighted average grain orientation spread. T_{BK}—two-pyroxene thermometer of Brey and Köhler (1990); T_{NG}—Ca-in-orthopyroxene thermometer of Brey and Köhler (1990) modified by Nimis and Grütter (2010); T_{REE}—REE thermometer of Liang et al. (2013). N/A = not applicable.

Three major textural types have been identified. *Granular textures* (Figure 1c) are dominated by curved to lobate grain boundaries for both olivine and pyroxenes, uniform grain size distributions, and lack of grain elongation. Pyroxene grain size often exceeds or shows a wider range than olivine. Pyroxene and spinel are generally dispersed instead of forming clusters, unlike the characteristic feature of protogranular textures (Mercier & Nicolas, 1975). *Porphyroclastic textures* (Figure 1d) show well-defined bimodal grain populations for both olivine and pyroxenes. Elongated olivine grains often define a lineation. Porphyroclasts are frequently surrounded by neoblasts of the same phase forming a core-and-mantle microstructure. *Equigranular textures* (Figure 1e) have straight grain boundaries, often meeting at 120° triple junctions. Olivine grain sizes average 0.5 mm and can reach a maximum of 1 mm; pyroxene grains are usually smaller, generally <0.5 mm, and evenly dispersed.

Both granular and porphyroclastic textures show a wide range in grain size; therefore coarse-grained and fine-grained subgroups were distinguished within each type. In the coarse-grained subgroup of granular (i.e., *coarse granular*) and porphyroclastic (i.e., *coarse-grained porphyroclastic*) xenoliths, the maximum grain sizes attain 5–6 mm for orthopyroxene and 3–4 mm for olivine and rarely 3 mm for clinopyroxene. Coarse orthopyroxene grains may contain clinopyroxene lamellae. Olivine and clinopyroxene sometimes appear as inclusions in orthopyroxene (e.g., NPY1311, NFL1324, and NFK1123), leading to poikilitic textures (Mercier, 1977). Spinel inclusions in olivine suggest grain growth (Mercier & Nicolas, 1975). In the fine-grained subgroup of granular (i.e., *fine granular*) and porphyroclastic (i.e., *fine-grained porphyroclastic*) xenoliths, the mean size of olivine is below ~800 μm, and the maximum grain size rarely exceeds 1 mm for olivine and 3 mm for pyroxenes.

These xenolith textures occur in different proportions in the different domains of the NGVF (Figure 1b). In the northern part, granular textures are dominant (62%), with equal proportions of coarse- and fine granular types. The remainder of the xenoliths (38%) are porphyroclastic, with 7% and 31% of coarse and fine porphyroclastic textures, respectively. In the central part, porphyroclastic textures are more abundant (47%, with 20% and 27% of coarse and fine subgroups, respectively) than granular ones (43%, with 23% and 20% of coarse- and fine-grained textures, respectively). A small proportion of xenoliths with equigranular textures (10%) is also present. In the northern and central part, both coarse and fine-grained microstructures are observed. In the southern part, grain size is significantly smaller, and the textures are fine porphyroclastic and equigranular (50%–50%).

In a few xenoliths from the Mašková and Jelšovec localities in the northern part and from the Fil'kovo Kerčik monovolcano in the central part, amphibole is present in low abundance (maximum 2%; Table 1). It usually appears as sparse interstitial grains and, in some cases, forms veins (see Figure 3 of Liptai et al., 2017). No amphibole was observed in the studied xenoliths from the other localities; however, Szabó and Taylor (1994) have described amphibole (2%–4%) in xenoliths from the central and southern part. Xenoliths from the southern localities may contain 0.5- to 1.5-mm wide melt pockets, consisting of glass and secondary clinopyroxene and spinel.

Deformation microstructures are observed in most xenoliths. They include a lineation denoted by alignment of spinel grains and, in the porphyroclastic peridotites, by elongated olivine porphyroclasts with aspect ratios up to 3:1 (Figures 2a and 2b). Olivine has undulatory extinction and subgrain boundaries (Figure 2c) in all textural types except for equigranular ones. In elongated olivines, subgrain boundaries are frequently at high angle to the elongation direction (Figure 2d). In a few xenoliths (NFL1315A, NFL1316, NMM1115, NBN0302A, and NBN0321), olivine- and pyroxene-rich domains define a diffuse compositional banding subparallel to the foliation defined by the olivine flattening. Olivine grain sizes (0.5–1.0 mm) are smaller in the pyroxene-rich domains than in olivine-rich ones, where olivine grains attain up to 1–2 mm in diameter (Figure 2e). Annealed microstructures are characteristic in equigranular and, to a lesser degree, in some porphyroclastic xenoliths, and they are represented by a decreased abundance of subgrain boundaries and low intragranular misorientations coupled to straight grain boundaries that meet at 120° triple junctions (Figure 2f).

To characterize the extent of intragranular misorientation resulting from stored dislocations in olivine, we determined the GOS, which defines the average spread in the difference between the orientation of each measurement point and the mean orientation of the grain (Wright et al., 2011, and references therein). Examples of high and low intragranular misorientations in the NGVF xenoliths are shown in Figures 2g

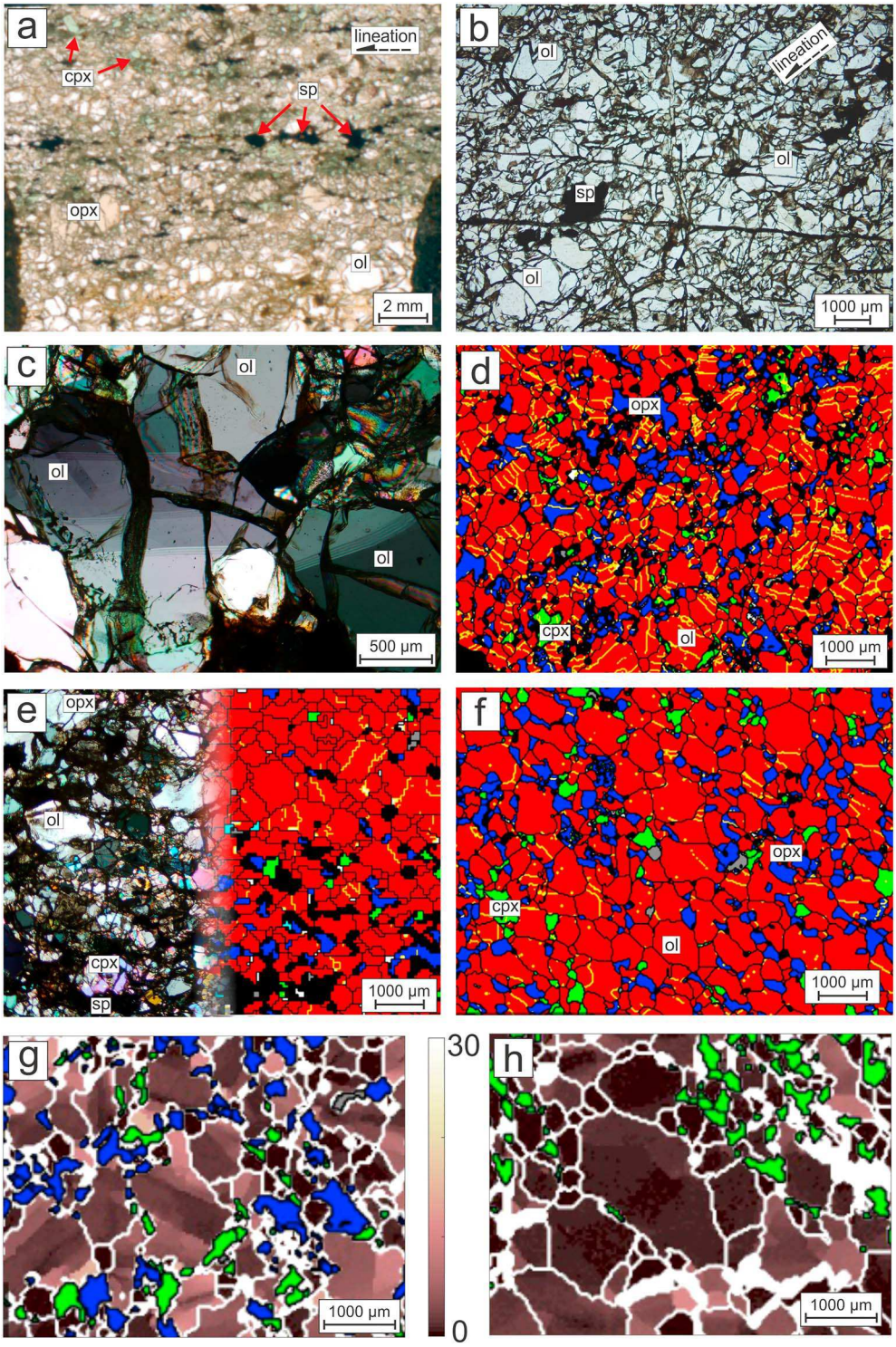

Figure 2. Characteristic microstructures in the studied Nógrád-Gömör xenoliths. (a) Lineation indicated by the distribution of spinel grains; (b) elongated olivine grains marking the lineation in a fine porphyroclastic xenolith; (c) olivine in a granular textured xenolith with well-developed subgrain boundaries; (d) EBSD phase map of a granular lherzolite with frequent subgrain boundaries (yellow) in olivine; (e) different olivine grain sizes in pyroxene-rich and pyroxene-poor domains in a porphyroclastic xenolith; microphotograph (left) and EBSD phase map (right); (f) equilibrated texture (straight grain boundaries, 120° triple junctions) in an equigranular xenolith; (g, h) "Mis-to-mean" (M2M; Wright et al., 2011) maps for olivine, where the color scale indicates the deviation of each measurement point from the average orientation of the grain expressed in degrees, illustrating peridotites with high (g) and low (h) degrees of intragranular misorientation in olivine. Photomicrographs are transmitted light, plane-polarized in a and b, and cross polarized in (c) and (e). EBSD phase maps: red—olivine, dark blue—orthopyroxene, green—clinopyroxene, grey—spinel, light blue—amphibole. Abbreviations: ol—olivine, opx—orthopyroxene, cpx—clinopyroxene, sp—spinel.

and 2h, respectively. Average olivine GOS values were calculated for each xenolith as area-weighted GOS averages of the individual grains (Table 1). Average olivine GOS values vary more with sampling locality rather than with textural type, but equigranular peridotites systematically show low average GOS (Figure S1a in the supporting information). Xenoliths from the northern part show the highest average olivine GOS values (2.1–3.2); those from the central part have intermediate average GOS (1.3–2.4), and the southern part xenoliths have the lowest values (1.1–1.6; Table 1).

6. Crystal Preferred Orientation

In the NGVF xenoliths, olivine shows all the three most widespread CPO symmetry types described in the lithospheric mantle worldwide: A-type orthorhombic, [010]-fiber, and [100]-fiber (Tommasi & Vauchez, 2015). Representative pole figures for each NGVF domain are shown in Figure 3a (see Figure S2 in the supporting information for pole figures of all xenoliths analyzed in this study) along with seismic properties calculated from CPO data and averaged for the whole volcanic field (Figure 3b; see Figure S3 in the supporting information for seismic properties of individual xenoliths). Most of the studied xenoliths do not have clear end-member CPO types but present transitional symmetries with a predominance of orthorhombic and [010]-fiber types (>90% of the total samples as determined by BA indices, Figures 4a and 4b). In peridotites with clear macroscopic lineation and foliation, the [100] axes of olivine cluster in a maximum parallel to the lineation in the foliation plane (A-type orthorhombic and [100]-fiber) or spread in a girdle in the plane of foliation with a weak maximum parallel to the lineation ([010]-fiber). The [010] axes tend to cluster normal to the plane of foliation in A-type orthorhombic and [010]-fiber CPO symmetries and are distributed in a girdle in a plane normal to the [100] direction with a weak maximum normal to the foliation in the rare samples with [100]-fiber olivine CPO pattern (Figure 3a). The [001] axes usually have a weak maximum normal to the lineation in the foliation plane with some dispersion either in the plane normal to the [010] maximum (A-type orthorhombic and [010]-fiber) or in the plane normal to the [100] maximum ([100]-fiber).

The distribution of olivine CPO types is slightly different for each domain within the volcanic field. In the northern part, most xenoliths show [010]-fiber symmetries (Figures 4a and 4b) with BA indices lower than 0.35 (Table 1), with two exceptions NMS1304 (BA = 0.66) and NJS1304 (BA = 0.45). In the central part, most peridotites have A-type orthorhombic CPO symmetry (17 xenoliths), followed by [010]-fiber (12 xenoliths; Figures 4a and 4b), and only one sample has [100]-fiber symmetry (NFK0301; BA = 0.75). Xenoliths from the southern part show a wide range of BA index and the olivine CPO symmetry correlates with the texture: peridotites with fine porphyroclastic textures tend to have [010]-fiber to orthorhombic CPO (BA indices of 0.09–0.44), whereas equigranular ones have orthorhombic to [100]-fiber CPO (BA indices of 0.59–0.70). In the northern and central localities, no clear correlation is observable between textural type and olivine CPO symmetry. However, granular and porphyroclastic xenoliths tend to show [010]-fiber and orthorhombic symmetries with lower BA indices, whereas equigranular ones tend to have higher BA indices (orthorhombic and [100]-fiber symmetries).

The intensity of the olivine CPO in the NGVF xenoliths, characterized by the J index (Bunge, 1982) (Table 1), also varies as a function of texture and locality. In the northern and central parts, J indices display similar ranges (2.1–4.9 and 2.4–4.9, respectively; Figures 4c–4e), except for two outliers (NTB1124 and NMM1126) where the low number of analyzed grains distorted the calculation and resulted in values over 6. Coarse granular and coarse porphyroclastic peridotites show on average higher J indices than fine granular and fine porphyroclastic ones; an exception is a fine porphyroclastic peridotite (NMS1302A), which has a J index of 4.6. In the southern part, olivine J indices range from 1.6 to 2.3, being significantly lower than the values in the northern and central part (Figures 4c–4e). Furthermore, equigranular-textured xenoliths of the southern part show lower J indices (1.6–1.8) compared to fine porphyroclastic ones (1.8–2.3). Olivine J indices show a positive correlation with equilibration temperatures determined using major element-based thermometers (Figure 4d). In contrast, the relation between olivine J indices and temperatures calculated from the REE distribution between orthopyroxene and clinopyroxene (Liang et al., 2013) displays a strong scatter (Figure 4e).

Orthopyroxene CPOs are generally weaker and show more scattered patterns than olivine. They sometimes show strong clustering at random directions (Figure 3a), which can be explained by the lower volume

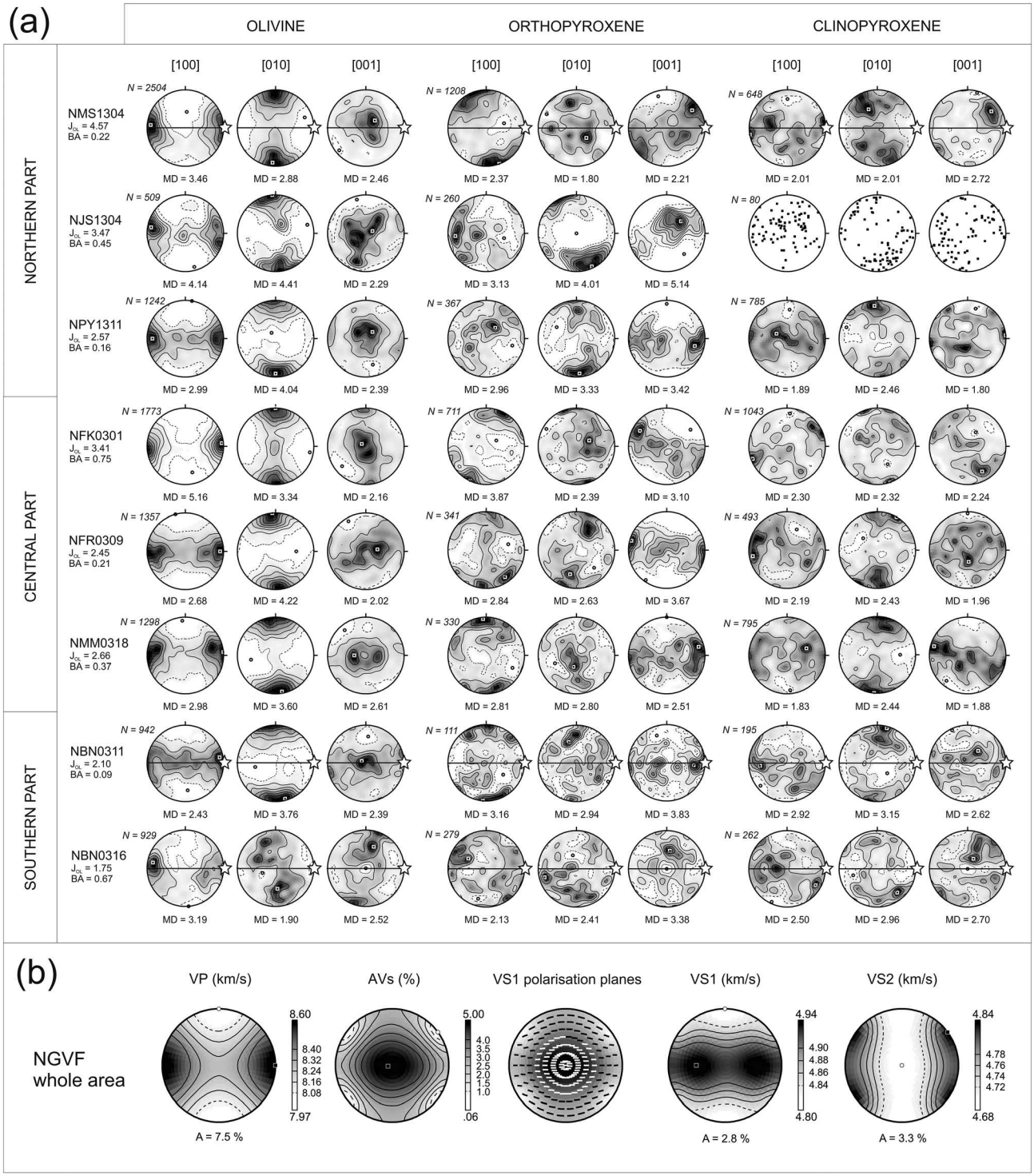

Figure 3. (a) Crystal preferred orientations of olivine and pyroxenes in representative xenoliths from the different parts of the volcanic field. Pole figures are lower hemisphere, equal area projections, in which the average orientations of all grains are plotted (one point per grain) and contoured at 0.5 multiples of uniform distribution. Maximum and minimum densities are indicated with a black square and a white circle, respectively; dashed line marks the lowest-value (0.5) contour. Where observable in the xenoliths, bold black line indicates the foliation and white star marks the stretching lineation. (b) Calculated average seismic properties at ambient temperature and pressure conditions for the Nógrád-Gömör Volcanic Field (NGVF). Lower hemisphere, equal area stereographic projections presented relative to the structural framework of the samples (lineation and foliation). VP, VS1, and VS2 are the 3-D distributions of *P* wave, fast and slow *S* wave velocities, respectively, the maximum propagation anisotropy is indicated at the bottom of each plot; AVs is the 3-D distribution of the polarization anisotropy of *S* waves (*S* wave splitting); VS1 (fast *S* wave) polarization planes are displayed as a function of the orientation of the incoming wave.

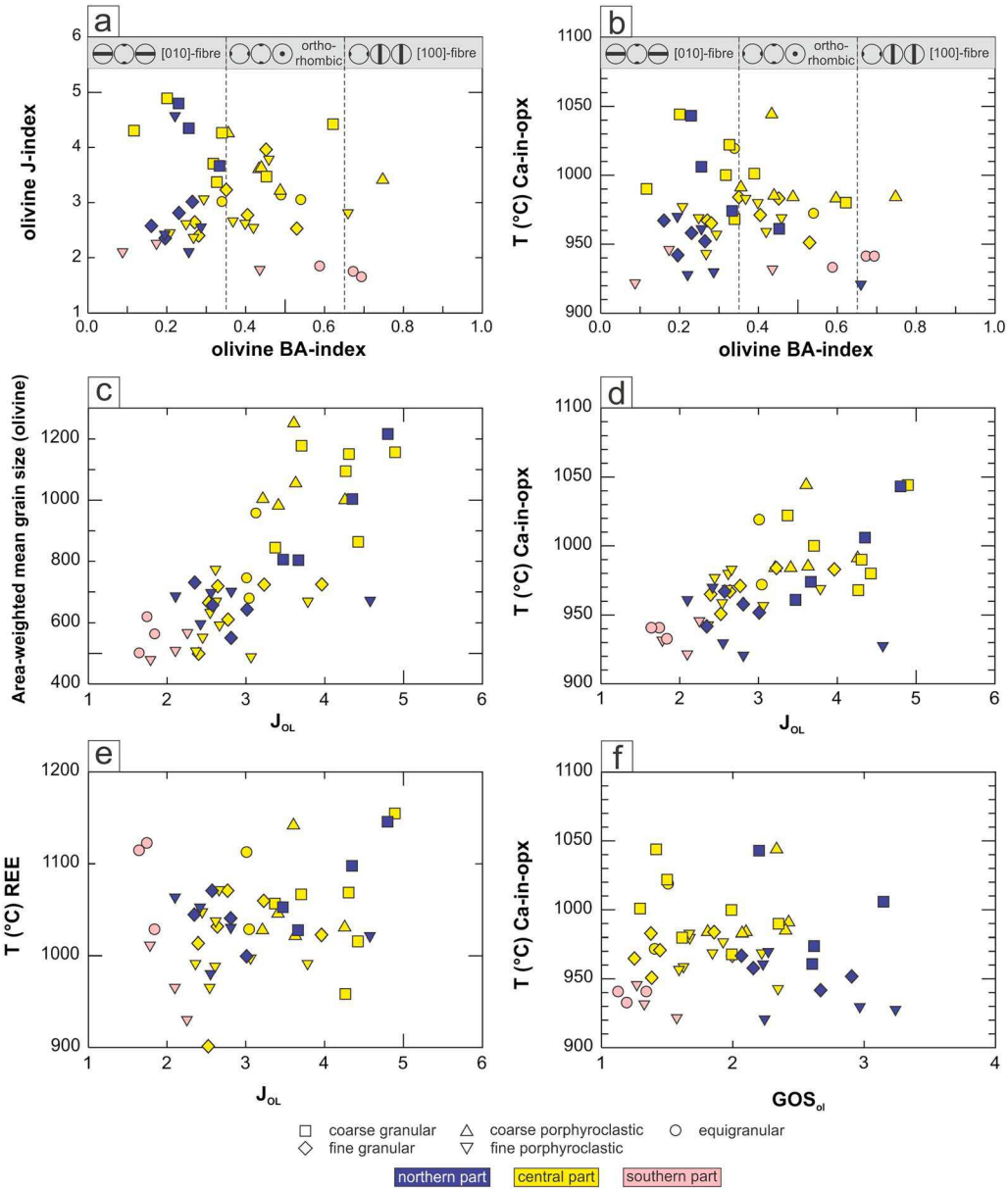

Figure 4. Comparative plots of the olivine deformation features (intensity and symmetry of the crystal preferred orientation and average intragranular misorientation) and equilibration temperatures (Liptai et al., 2017). Applied thermometers: Ca-in-opx thermometer of Brey and Köhler (1990) modified by Nimis and Grütter (2010); REE-thermometer of Liang et al. (2013).

fraction and larger sizes of pyroxenes, which makes it difficult to obtain a representative number of measurements in a thin section. Furthermore, late brittle fracturing and minor alteration lead to imprecise identification of larger grains and result in an overrepresentation of similarly oriented grain fragments in the one-point-per-grain data set. In peridotites with a clear foliation and lineation, the maximum density of orthopyroxene [001] axes is concentrated at a low angle to the lineation, subparallel to olivine [100] axes and [100] axes of orthopyroxene are often normal to the foliation plane. This correlation between olivine and orthopyroxene CPO is present in the randomly cut xenoliths as well. In these xenoliths, orthopyroxene axes show clearly observable maxima, suggesting that CPO patterns of all xenoliths have the same relationship with the foliation and lineation. This justifies the rotation of the samples into a common reference frame, in which the maximum of olivine [100] defines the lineation

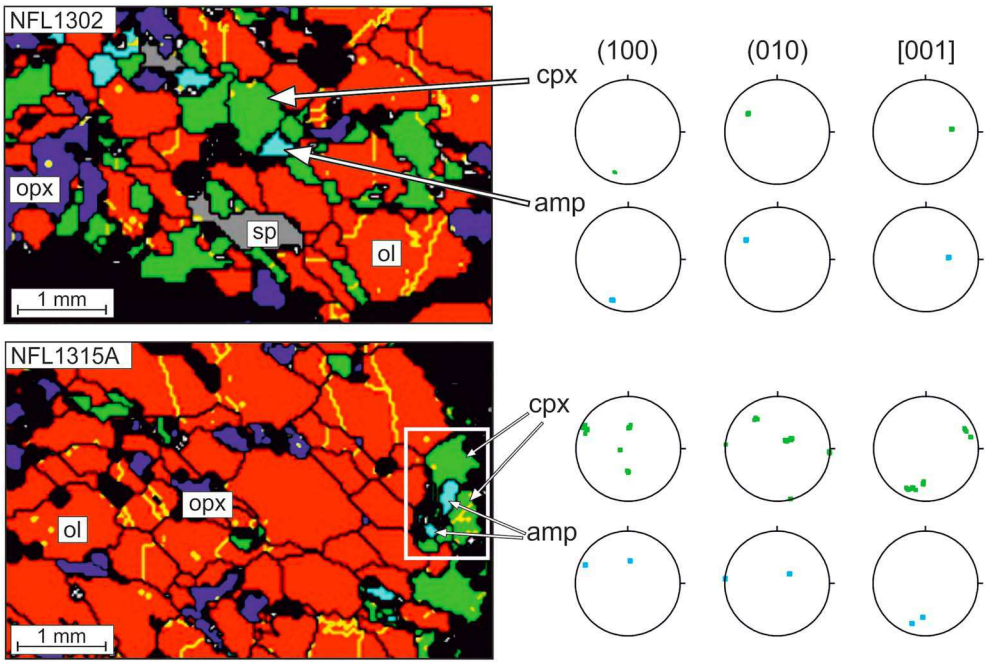

Figure 5. Examples of amphibole grains displaying matching orientation with neighboring clinopyroxenes. Phase colors are the same as on Figure 2.

(E-W direction in the pole figures) and the maximum of olivine [010] the pole to the foliation (N-S direction in the pole figures). Some dispersion of orthopyroxene [001] axes in the plane of the foliation is often observed, particularly in peridotites that have [010]-fiber olivine CPO patterns (Figure S2 in the supporting information). In 26% of the xenoliths the [001] and [100] axes of orthopyroxene are not aligned with the olivine [100] and [010] axes, respectively. In these xenoliths, orthopyroxene CPO is either nearly random (e.g., NBN0311 and NBN0316; Figure 3a) or characterized by [100] and [001] maxima aligned with the olivine [100] and [001] maxima, respectively (e.g., NFK1115; see Figure S2 in the supporting information).

Clinopyroxene crystallographic axes are more dispersed than those of orthopyroxene and in most peridotites no clear CPO is observable. Where a well-developed CPO is present, it tends to be similar to the orthopyroxene CPO, with [001] axes aligned or at a small angle to the olivine [100] maximum. In a few xenoliths (e.g., NFR0309 and NMM0318), clinopyroxene has weak CPO with orientation of [100] and [010] axes aligned with the olivine [100] and [010] axes, respectively (and to the orthopyroxene [001] and [100] axes, respectively).

The low modal amount of amphibole in the NGVF peridotites (Table 1) does not allow for the statistical analysis of their CPO. However, at the grain scale, amphibole CPO in several xenoliths from Fil'akovo-Kerčik locality (NFL1302, NFL1315A, NFL1324, and NFL1326) is similar to that of neighboring clinopyroxene (Figure 5).

7. Seismic Properties

Calculated seismic properties of individual xenoliths share similar characteristics as shown for the average seismic properties for all NGVF peridotites in Figure 3b. The *P* wave propagation is fastest in a direction close to the strongest olivine [100] axis concentration, that is, the direction of the lineation, and slowest in a direction normal to the foliation plane (i.e., olivine [010] maxima in most xenoliths). The *P* wave anisotropy in the average sample reaches a maximum of 7.5% for waves propagating in a plane containing the lineation and the normal to the foliation (Table 1). The fast-split *S* wave (S1) is polarized in a plane that contains the propagation direction and the lineation. The maximum *S* wave anisotropy (4.9% on average, but ranging from 2.9% to 8.0% in individual samples; Table 1) is observed for propagation in the plane of

foliation, but perpendicular to the lineation. The maximum velocities of fast S1 waves are in a direction within the plane of foliation, at ~45° to the lineation, and the slowest S1 propagation is normal to the foliation. The slow *S* wave (S2) shows high velocities within 45° to both the lineation and the foliation plane.

8. Discussion

8.1. Microstructural Evolution of the Nógrád-Gömör Xenoliths

The mantle xenolith suite of the NGVF displays clear olivine CPOs (Figure 3a) with low to intermediate fabric strength (J_{OL} = 1.6–4.9), as well as abundant signs of intracrystalline deformation in olivine, such as undulatory extinction, grain elongation, and subgrain boundaries often perpendicular to the grain elongation, which marks the stretching direction (e.g., Figure 2b). These features are interpreted as results of deformation by dislocation creep, which is the dominant deformation mechanism in coarse-grained peridotites at high-temperature upper-mantle conditions (e.g., Green & Radcliffe, 1972; Mercier & Nicolas, 1975).

The strong orientation of olivine [100] axes in most xenoliths indicates that slip in the [100] direction was dominant during the deformation. Orthopyroxene [001] axes cluster parallel to or at a small angle to olivine [100] axes, which suggests coeval deformation of olivine and orthopyroxene and dominant [001] slip in orthopyroxene. Most NGVF xenoliths display [010]-fiber and A-type orthorhombic olivine CPO patterns; only a few samples have [100]-fiber symmetries (see BA indices in Table 1). There is no correlation between equilibration temperatures and CPO patterns (Figure 4b), and olivine BA indices show a continuous distribution between the different symmetries (Figures 4a and 4b). Furthermore, no clear link is observed between textural types and CPO symmetry. Although equigranular xenoliths tend to have higher BA indices (i.e., mostly orthorhombic and [100]-fiber patterns; Figures 4a and 4b), granular- and porphyroclastic-textured samples show wide variability in CPO types and intensity. The observed CPO patterns are in agreement with deformation under dry conditions, which is supported by a recent study on structural hydroxyl content of the nominally anhydrous minerals in the NGVF xenoliths (Patkó et al., 2019). They observed that the olivine and pyroxenes of the xenoliths are extremely dry and proposed that this can be explained by major hydrogen loss during the extensional phase, due to decompression-driven decrease in the activity of "water."

Peridotites with [010]-fiber olivine CPO symmetries are more abundant (~50%) in the NGVF than worldwide (15% in the database of Ben Ismail & Mainprice, 1998). The formation of this CPO symmetry is interpreted as a result of (1) axial shortening or transpression (Tommasi et al., 1999), (2) simultaneous activation of [100] and [001] glide at high pressure, high stress, or low temperature (Demouchy et al., 2013; Mainprice et al., 2005; Vauchez et al., 2005), (3) deformation in the presence of melt (Higgie & Tommasi, 2012; Holtzman et al., 2003), or (4) CPO evolution in response to dynamic or static recrystallization (Falus et al., 2011; Tommasi et al., 2008). In the NGVF, xenoliths with [010]-fiber symmetries do not show systematically lower equilibration temperatures (Figure 4b) nor any textural evidence of having been exposed to higher stresses than the rest of the suite, as this CPO group contains both fine- and coarse-grained peridotites with variable J index values (Figure 4a). Deformation in the presence of melt cannot be excluded unambiguously since metasomatic melts were present in the NGVF upper mantle following the Miocene extension (Liptai et al., 2017). However, there is no simple relation between the intensity of the metasomatic imprint, characterized by changes in the modal and/or chemical composition (Liptai et al., 2017). Similarly, there is no clear link between more pronounced annealing structures and [010]-fiber CPO. Indeed, the equigranular xenoliths, which have the most recrystallized microstructure and lowest GOS values, have olivine CPO with a [100]-fiber tendency (Figures 4a–4f). This observation does not corroborate dynamic or static recrystallization as the main explanation for the development of [010]-fiber olivine CPO. In most xenoliths, both olivine [100] and orthopyroxene [001] axes, which represent the dominant glide direction in the two minerals, show dispersion in the foliation plane (Figures 3a and S2 in the supporting information). We interpret this as an evidence of transpression (e.g., Tommasi et al., 2006; Vauchez & Garrido, 2001). However, while this seems to be a plausible explanation for the development of [010]-fiber olivine CPO, additional factors, such as recrystallization or the presence of melts during deformation, may have also contributed locally. It has to be noted that in very fine grained materials such as mylonites, the increasing effect of grain boundary sliding in the deformation mechanism was also attributed to result in [010]-fiber olivine CPO, as described by Précigout and Hirth (2014) in the Ronda peridotite. However, even the fine-grained NGVF xenoliths have

grain sizes (500–800 μm; Figure 4c), which exclude grain boundary sliding in upper mantle *P-T* conditions (e.g., Kohlstedt, 2007).

A-type orthorhombic CPO or orthorhombic CPO with a slight [100]-fiber tendency, which characterize the other half of studied xenoliths (Figures 3a and 4a and 4b), are produced by dominant activation of the (010) [100] slip system in simple shear, pure shear, or a 2-D combination of these regimes, that is, plane transpression or plane transtension (Tommasi et al., 1999, 2000). Since the xenoliths display a continuous variation in olivine CPO symmetry between [010]-fiber and orthorhombic with a [100]-fiber tendency, with no clear relation with either textural type or equilibration temperatures, we propose that the changes in olivine CPO symmetry result from spatial variations in the deformation regime, from dominant shear to transpression, and maybe locally from the presence of melt during the deformation.

In addition to the microstructural evidence for deformation by dislocation creep (e.g., clear CPO and subgrain boundaries), xenoliths from the central and southern part of NGVF often display low density of subgrains and of stored dislocations in olivine, characterized by low intragranular misorientation (Figure 4f; GOS values below ~1.7 are often interpreted as characteristic of annealed texture; e.g., Aradi et al., 2017; Hidas et al., 2016), straight grain boundaries, and 120° triple junctions (Figure 2f). These microstructural features indicate that the recrystallization probably was postkinematic (annealing), leading to recovery within the grains and some grain boundary migration (e.g., Bestmann et al., 2005; Borthwick & Piazolo, 2010). The predominance of low J indices in fine-grained xenoliths relatively to coarse-grained ones (Figure 4c) points to dispersion of the CPO only when recrystallization produces grain size reduction, consistently with previous observations by Falus et al. (2011). When it results in grain growth, annealing may preserve or even increase the strength of the olivine CPO (e.g., Tommasi et al., 2008; Vauchez & Garrido, 2001). This may explain the very weak correlation between GOS and J index (Figure S1b in the supporting information). Furthermore, in xenoliths with a diffuse compositional layering, olivine grains are larger in olivine-rich domains than in pyroxene-rich domains (Figure 2e), suggesting pinning of olivine grain boundaries by the pyroxenes (Herwegh et al., 2011).

In the NGVF xenoliths, GOS values vary distinctly among the different subareas (Figure 4f), being higher in the northern part and lower in the southern. However, there is no clear correlation between GOS and textural types, except for the very low GOS values of equigranular peridotites. This might be explained by the complex interplay between deformation and annealing. Indeed, the stored dislocation density and hence the amount of intragranular misorientation is proportional to stress during deformation, whereas both dynamic recrystallization and annealing lead to a decrease in dislocation density. The spatial variation of GOS values probably indicates lateral and/or depth-dependent changes in the deformation-annealing histories for the three domains.

8.2. Spatiotemporal Evolution of the Textures in the Lithospheric Mantle Beneath the NGVF

Coarse granular and coarse porphyroclastic xenoliths typically have higher fabric strength and higher equilibration temperatures than fine granular, fine porphyroclastic, and equigranular ones (Figures 4c and 4d). Both coarse and fine grained groups are well represented in the northern and central areas, while in the southern part, all xenoliths belong to the low-temperature, fine-grained group. If the equilibrium temperatures record a stable geotherm at the time of the extraction of the xenoliths, which may not be the case for the more metasomatized central area, but is an acceptable hypotheses for the other two domains, these two groups may represent sampling of different depths of the lithospheric mantle beneath NGVF.

The low Ca-in-opx equilibration temperatures of the equigranular peridotites in the southern domain contrast with their well-annealed microstructures. These xenoliths record nevertheless significantly higher REE-based equilibration temperatures (Figure 4e), which are interpreted to represent older, hotter mantle conditions, probably linked to the Miocene extension and asthenospheric uplift (Liptai et al., 2017). We interpret therefore these microstructures as recording deformation and annealing in the shallow lithospheric mantle related to the Miocene extension, which was followed by cooling. The less annealed xenoliths from the northern area show variable Ca-in-opx equilibration temperatures, which are nevertheless on average higher than those of the xenoliths from the southern area (Figure 4f). This points to a more recent deformation. The only major geodynamic event postdating the extension is the tectonic inversion and the onset of the compressional tectonics resulting from the convergence and rotation of the Adria microplate (Bada et al.,

2007; Horváth & Cloetingh, 1996). These xenoliths also show dominantly [010]-fiber olivine CPO (Figures 4a and Table 1). We therefore propose that the olivine CPO of the xenoliths from the northern domain records this recent compressional-transpressional stress field. Note that equilibration temperatures at the time of sampling by the host magma probably do not correspond to the deformation temperature, which is likely higher and thus somewhere between the values given by the Ca-in-opx and the REE-based thermometers.

Finally, the xenoliths from the central NGVF show low GOS, high Ca-in-opx equilibration temperatures (Figure 4f), which are in many cases similar to the REE-based ones (Figure 4e), and highly variable olivine CPO symmetry and intensity (Figure 4a) and grain size (Figure 4c). This points to annealing of a mantle section submitted to heterogeneous deformation. In the geodynamic evolution of the Pannonian Basin, there are several possibilities for annealing the subcontinental lithospheric mantle. The Miocene extension and accompanying asthenosphere uplift (e.g., Horváth, 1993; Stegena et al., 1975) certainly resulted in heating of the lithospheric mantle, as recorded by the high REE-based equilibration temperatures (Figure 4e). Annealing could also be post-Miocene. A way to produce local heating and annealing in the lithospheric mantle is by melt percolation. Melt-induced annealing has been described in studies of xenolith suites in the Eastern Betics in SE Iberia (Hidas et al., 2016; Rampone et al., 2010), the Hoggar swell in Algeria (Kourim et al., 2015), and the Styrian Basin in the western CPR (Aradi et al., 2017), where microstructural or geochemical evidence (e.g., amphibole formation) points to melt-rock interaction.

In the NGVF, microstructural evidence for melt-induced annealing is scarce. However, Liptai et al. (2017) has recognized three distinct metasomatic events as summarized in section 3. The first of these metasomatic events probably is older than the Miocene extension, but the last two involve melts that are assumed to have percolated in the upper mantle of the NGVF after the extension, just prior to the eruption of the host basalt. The second metasomatic event appears to be the most widespread, affecting the upper mantle under all three parts of the NGVF. Evidence for this metasomatism mostly appears only in geochemical data, without petrographic signs, except for the Nb-rich amphiboles, which are only present in a few xenoliths. Nevertheless, most of these amphiboles tend to show CPO matching those of adjacent clinopyroxenes (Figure 5). Such microstructural relationships between amphibole and clinopyroxene have been described in the Lanzo orogenic peridotite (Kaczmarek & Tommasi, 2011), in peridotite xenoliths from the Hoggar swell (Algeria; Kourim et al., 2015), and from the Styrian Basin (Aradi et al., 2017) and have been interpreted as reflecting nucleation of amphibole on preexisting, deformed clinopyroxene during late-stage modal metasomatism. Consequently, the Nb-rich amphiboles in the NGVF support the suggestion that metasomatizing melts infiltrated the upper mantle subsequent to, or at a late stage of, the main deformation that produced the clinopyroxene CPO. The third (i.e., the youngest) metasomatic event was only active under the central part of the NGVF (Liptai et al., 2017; Figure 1b), as supported by the lack of xenoliths carrying wehrlitic signature in the northern and southern parts. The presence of a reacting melt under the central part shortly before the eruption of the host basalt (Novák et al., 2014) may explain the higher equilibration temperatures observed in the xenoliths from this domain (Figure 4f).

Thus, we propose that annealing in the SCLM of the NGVF was favored by percolating and reacting melts and associated heating. Melt pockets are common in xenoliths of the southern part, and less abundant in xenoliths from the northern and central part: they are interpreted to result from in situ melting of reacting amphibole (Liptai et al., 2017), further supporting local but effective heating. However, it is not possible to constrain the timing of this amphibole breakdown, which may be associated with the extraction process. Moreover, in the southern part, major element-based equilibration temperatures are low; thus, annealing might have been associated with melt percolation, but the latter must be an older process. In contrast, in the central part, the mantle retained higher temperatures, recorded by the major element thermometers (Table 1), probably due to a recent and more extensive exposure to percolating melts related to the formation of wehrlites.

8.3. Seismic Properties of the NGVF Lithospheric Mantle

The presence of clear CPO in the xenoliths of the NGVF indicates that at least part of the SKS splitting measured in this region should reflect fossil deformation in the lithospheric mantle (e.g., Tommasi & Vauchez, 2015). Using the average seismic properties calculated based on the CPO and modal compositions of the studied xenoliths (Figure 3b), we have estimated the thickness of lithospheric mantle under the NGVF

required to explain the measured shear wave splitting, assuming a single layer with homogeneous orientations of foliation and lineation (grain boundaries and hence the variations in grain size shown by the xenoliths do affect seismic attenuation, but not seismic anisotropy). Since the measured delay time between fast and slow polarized component of the vertically propagating SKS waves depends heavily on the orientation of the foliation and lineation, the end-member cases of Baptiste and Tommasi (2014) were considered for the calculation (Figure S4 in the supporting information). The five end-member cases are horizontal foliation and lineation (case 1), vertical foliation and horizontal lineation (case 2), vertical foliation and lineation (case 3), 45° dipping foliation and lineation (case 4), and 45° dipping foliation and horizontal lineation (case 5). Based on observations at the three seismological stations closest to the NGVF (see Figure 3 of Klébesz et al., 2015), an average SKS wave delay time of 1.3 s was considered.

Anisotropy in the crust may contribute to SKS delay times; on average a delay time of 0.1–0.2 s may be accumulated in a 10-km thick crustal section (Barruol & Mainprice, 1993). Assuming a ~25-km thick crust for the NGVF (Klébesz et al., 2015), ~0.25 s of delay time may be produced in the crust. Thus, if the crust and mantle contributions are additive, at least 1.05 s of delay time should be produced in the mantle, implying an anisotropic mantle layer with minimum thicknesses of 181, 101, 227, 1,017, and 143 km for cases 1–5, respectively. The global average maximum depth where CPO-induced seismic anisotropy is strong is ~250 km (Mainprice et al., 2005), so a value of 1017 km is unrealistic. The remaining values are all lower than the corresponding thicknesses of the anisotropic layer for each case calculated by Klébesz et al. (2015), which used xenoliths exclusively from the southern part of the NGVF, that have weaker olivine CPO (Figure 4a) and did not separate crustal and mantle components in the delay time.

The direction of fast-polarized *S* waves near the NGVF is oriented NW-SE (Dando et al., 2011; Qorbani et al., 2016; Stuart et al., 2007). This is consistent with the present-day stress field in the CPR, which records the tectonic inversion and NE-SW compression caused by the convergence of the Adria microplate and the European platform since the late Miocene (Bada et al., 2007). The average lineation in the anisotropic mantle layer should be normal to the compression, that is, parallel to NW-SE direction. This excludes the possibility of case 3 (vertical foliation and lineation), which leaves the options of horizontal, vertical, or dipping foliation with a lineation with a NW-SE trend. A horizontal foliation would require the thickest anisotropic layer, and a vertical foliation would require the thinnest layer to produce the observed 1.3-s delay time. A vertical foliation with a horizontal lineation (case 2), which allows the vertically propagating core *S* wave to sample most anisotropic direction in the mantle layer, requires a thickness of 101 km to produce 1.05 s of SKS splitting. Thus, if a 25-km thick crust is assumed, the minimum thickness of the anisotropic layer in the NGVF is ~125 km.

The depth to the lithosphere-asthenosphere boundary (LAB) beneath the NGVF has been estimated by several studies. Klébesz et al. (2015) used a receiver function approach and placed the LAB at ~ 65 $\pm$ 10 km. Tašárová et al. (2009) using 3-D gravity modeling estimated a lithospheric thickness in this region of ~80–100 km. Bielik et al. (2010) suggested an even thicker lithosphere of ~100–120 km using integrated 2-D modeling of gravity, geoid, topography, and surface heat flow data. If the unusually thin lithosphere thickness of ~65 km inferred by Klébesz et al. (2015) applies, then a minimum of ~60 km of sublithospheric mantle with coherent seismic anisotropy is required to produce the observed delay times. The LAB depth estimates of Tašárová et al. (2009) would require a minimum of ~25 km of asthenospheric contribution. A scenario, where all SKS splitting is produced in the lithosphere, would only be possible if the foliation in the lithospheric mantle was vertical and the LAB was at ~125-km depth beneath the NGVF (case 2 with crustal contribution included). Although such LAB depths have been proposed as maximum values (Bielik et al., 2010), it may be shallower than this (Tašárová et al., 2009). Moreover, absence of an asthenospheric contribution to seismic anisotropy is not a plausible hypothesis. The uniform SKS fast-polarization directions despite the complex crustal structures of the region have indeed led Qorbani et al. (2016) to propose the presence of a sublithospheric anisotropic layer with a homogeneous NW-SE fabric under the CPR.

Therefore, we suggest that the observed seismic anisotropy is most likely partly produced in the asthenospheric mantle as it was proposed for the Styrian Basin (Aradi et al., 2017) and the central region of the Pannonian Basin (Little Hungarian Plain and Bakony-Balaton Highland; Kovács et al., 2012). In contrast, for the Perşani Mountains on the eastern margin of the CPR, Falus et al. (2008) concluded that assuming a vertical foliation, the observed delay times (~1 s) could entirely be attributed to the lithospheric mantle.

If a single layer in the lithospheric mantle is assumed, we favor a subvertical foliation and a shallowly dipping lineation. This would be consistent with transpressional deformation in response to the present-day stress field as the eruption of the xenolith-hosting basalts occurred after the change from extensional to compressional regime (~8 Ma; e.g., Horváth & Cloetingh, 1996), and the xenoliths are considered to have sampled the mantle in this tectonic environment. Furthermore, a vertical foliation could better accommodate the vertical migration of melts (Tommasi et al., 2006; Waff & Faul, 1992) and could provide a plausible explanation for the clearly NW-SE oriented distribution of the xenolith-hosting basalt fields on the surface (Figure 1b). However, it cannot be excluded that the orientation/dipping angle of the foliation may vary with depth as in large-scale shear zone systems (e.g., Vauchez et al., 2012).

8.4. Links to the Tectonic Evolution of the CPR

Both geochemical and crystallographic data on the studied xenoliths suggest that the upper mantle beneath the NGVF has a complex history. Due to overprint on the petrographic record, it is difficult to give a full reconstruction of the different metasomatic and deformation events. However, using previous constraints on the tectonic evolution of the CPR and results of studies on other CPR xenoliths, in addition to the present observations, we propose a conceptual model for the evolution of the mantle segment beneath the NGVF (Figure 6).

The last major deformation is the compression that followed the Miocene extension. The olivine CPO symmetry (characterized by the BA indices, Figures 3a and 4a and 4b) is consistent with transpression or simple or pure shear deformation regimes. The variations in olivine CPO symmetry do not directly correlate with textural types, nor with the provenance of the xenoliths within the NGVF. We suggest therefore that they record local variations in deformation regime. However, [010]-fiber textures and less annealed microstructures predominate among the xenoliths of the northern NGVF, consistently with interpretation of these textures as related to the most recent compressive deformation. Xenoliths from the southern and central localities show a higher frequency of microstructural features indicating annealing. In the central part, the xenoliths show high major-element-based equilibration temperatures and there is petrological and geochemical evidence for extensive melt percolation, which probably favored annealing. The lower major element temperatures of the xenoliths of the southern part may, on the other hand, imply that they represent remnants of an older event in the shallow lithospheric mantle. The increase of grain sizes and fabric strength with depth, observed among the NGVF xenoliths, is a general feature of the CPR as shown by studies on xenoliths from the Styrian Basin, Bakony-Balaton Highland, and Perşani Mountains. However, the tectonic environment for these xenolith occurrences is different, and it is important to compare the geodynamic situation of the NGVF to these other volcanic fields.

In the central part of the Pannonian Basin (Little Hungarian Plain and Bakony-Balaton Highland), Kovács et al. (2012) described a shallower layer with fine-grained porphyroclastic- and equigranular-textured xenoliths showing [010]-fiber CPO and a deeper layer with coarse-grained porphyroclastic xenoliths showing orthorhombic symmetries. The former group was interpreted to represent the uppermost lithospheric mantle of the ALCAPA microplate, which was deformed during the Alpine collision and extrusion, whereas the latter group was suggested to be the remnant of the east-west directed asthenospheric flow associated with the Miocene extension. These geochemically fertilized xenoliths represent asthenospheric mantle that became a part of the lower lithosphere during the postextensional thermal relaxation (Kovács et al., 2012). The affiliation with the asthenospheric flow is further supported by seismic data as fast-polarized *S* wave directions for the near vertically propagating SKS phase outline an east-west general direction in the central part of the Pannonian Basin (Dando et al., 2011; see Figure 5 of Kovács et al., 2012; Stuart et al., 2007). In the marginal zones of the CPR such as the Styrian Basin and the Perşani Mountains, the degree of extension and thus the asthenospheric uplift was less significant. Therefore, coarse-grained microstructures in these sites cannot be interpreted as fossil asthenosphere accreted to the lithosphere after the extension. Xenoliths from the Styrian Basin provide evidence for a major deformation event in a transpressional regime (Aradi et al., 2017), in agreement with the recent geodynamics of the western CPR, that is, the NE-directed subduction and rotation of the Adria microplate (Bada et al., 2007; Qorbani et al., 2016). In the Perşani Mountains, convergent plate tectonics (subduction/collision) dominates the deformation processes in the lithospheric mantle (Csontos, 1995; Falus et al., 2008). Both marginal areas show petrographic and geochemical evidence of percolating subduction-related fluids/melts (Aradi et al., 2017; Falus et al., 2008; Vaselli et al., 1995, 1996).

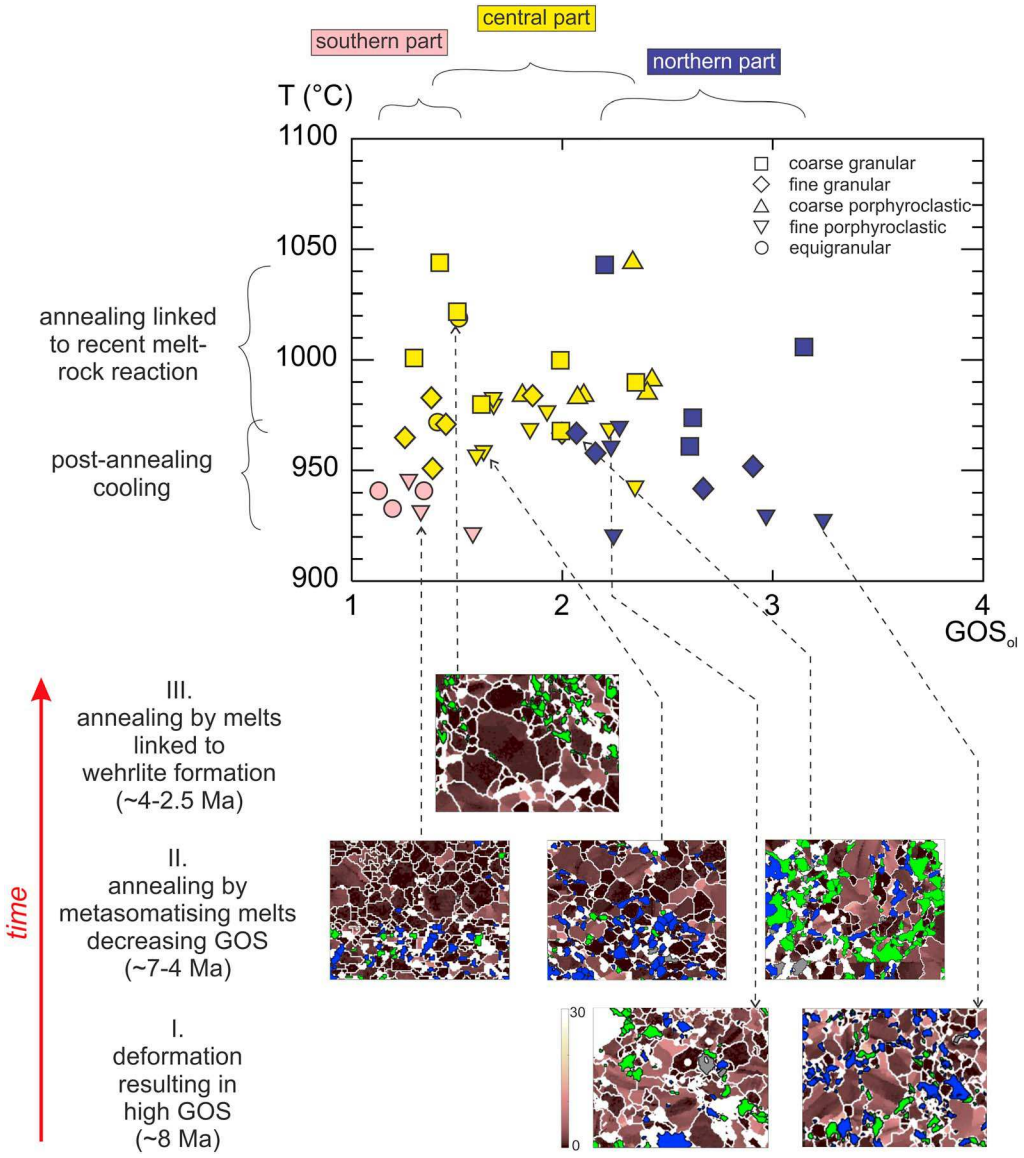

Figure 6. Reconstructed stages of deformation and annealing events in the Nógrád-Gömör lithospheric mantle based on microstructural characteristics and thermal conditions. I.—Deformation in a dominantly transpressional regime (beginning from ~8 Ma), leading to strong intragranular deformation manifested in high grain orientation spread (GOS); II.—Annealing linked to the heating effect of percolating metasomatizing mafic melts in the upper mantle (prior to the eruptions in the central part), resulting in grain growth and the decrease of intragranular deformation. III.—Annealing in the central part of the Nógrád-Gömör Volcanic Field, linked to the formation of the wehrlite suite (Patkó et al., 2013) shortly before and during the eruption of the host basalt in the central part. EBSD maps showing the transformation from deformed to annealed textures are "mis-to-mean" (M2M; Wright et al., 2011) maps for olivine, where the colour scale indicates the deviation of each measurement point from the average orientation of the grain. Colors of mineral phases other than olivine are the same as on Figure 2.

In the NGVF, there is no sign of recent subduction. However, the rare Nb-poor amphiboles described by Liptai et al. (2017) were interpreted as modal metasomatic products of a subduction-related fluid or hydrous melt, based on the criteria of Coltorti et al. (2007). These amphiboles were suggested to be the imprint of an older subduction predating the extrusion of the ALCAPA microplate (Kovács & Szabó, 2008; Liptai et al., 2017). Furthermore, the presence of a "lithospherized" mantle layer similar to the central part of the Pannonian Basin is not corroborated, as CPO patterns do not seem to correlate with depth. SKS fast-polarization directions also differ, being oriented NW-SE instead of E-W (Dando et al., 2011; Qorbani

et al., 2016; Stuart et al., 2007). The wide variety of CPO patterns suggests spatial variations in the deformation regime, among which transpression likely predominates, given the high abundance of [010]-fiber symmetries (Figures 4a and 4b) compared to the world average (Ben Ismail & Mainprice, 1998). This can probably be attributed to the effect of the convergence of the rotating Adria block and the European plate (Bada et al., 2007; Fodor et al., 1999; Horváth et al., 2006; e.g., Horváth & Cloetingh, 1996). A transpressional deformation was also suggested to explain the high abundance of [010]-fiber symmetries in the Styrian Basin (Aradi et al., 2017). This, along with recent measurements of SKS splitting showing high delay times, further supports the idea that the flow directions in the upper mantle are oriented NW-SE parallel to the fast polarization directions.

Since annealed microstructures overprint deformation in the xenoliths, annealing is suggested to have taken place after the onset of compressional tectonics. Although intraplate mafic melts are inferred to be mainly generated by the decompression during extension (Embey-Isztin et al., 1993), the eruption ages of the host basalts suggest that melt percolation and reaction with the peridotite wall rock also occurred during the post-extensional convergent tectonics. Melts already present in small quantities in the asthenosphere could have been squeezed upward upon the change of the foliation to subvertical (Kovács, Kiss, et al., 2018). Alternatively, the time gap between the active extensional phase and the ascent of asthenospheric melts may be explained by mantle convection patterns, as proposed in the numerical models of Balázs et al. (2017). However, heating by these melts must have happened earlier than xenolith entrapment and transport to the surface, as low equilibration temperatures in the northern and southern parts (Table 1 and Figure 6) suggest postannealing cooling, and thus are more likely to represent the depth of origin at the time of entrapment. Trepmann et al. (2013) showed that annealing of microstructures in natural peridotites can be achieved on a scale of tens to tens of thousands of years. Annealing by the host basalt can be excluded, as Szabó and Bodnar (1996) showed that the basalts transporting the xenoliths reached the surface from upper mantle depths in ~36 hr. The most recent annealing event is assumed to be associated with the formation of wehrlites (Liptai et al., 2017; Patkó et al., 2013), which is restricted to the central part only, where equilibration temperatures cover a significantly higher range (Figure 6). The fact that xenoliths from the central part retained these elevated temperatures suggests that the melt/wall-rock reaction leading to wehrlite formation was still occurring during host-basalt eruptions in the central part of the NGVF.

9. Conclusions

Alkali basalts in the Nógrád-Gömör Volcanic Field (NGVF) have sampled a laterally and vertically heterogeneous upper mantle segment in the northern part of the Pannonian Basin, an area submitted to a major extensional deformation, leading to marked thinning of the lithosphere during the Miocene and to a compressional/transpressional tectonic regime from late Miocene to recent times. The xenoliths record deformation, followed by variable degrees of annealing, which is least expressed in xenoliths from the north and best in those from the central and southern parts of the NGVF. Olivine CPO patterns indicate heterogeneous deformation, which was dominated by a transpressional regime, consistent with the recent tectonic environment of the Carpathian-Pannonian region. We suggest that annealing was favored by mafic melts of intraplate origin, which infiltrated and metasomatized the upper mantle following the onset of the convergent tectonics. The latest of these metasomatic events is reflected in the elevated equilibration temperatures of xenoliths from the central part of the volcanic field, which present widespread evidence for annealing.

The combined results of deformation and annealing processes resulted in a twofold heterogeneity: (1) the amount of intragranular deformation preserved in the olivine crystals decreases from the north toward the south and (2) in all domains of the volcanic field, shallower layers show more dispersed olivine crystal preferred orientation, whereas deeper layers have stronger fabrics. Comparison of the average seismic properties of the studied xenoliths to seismological data suggests that the lineation is most likely oriented NW-SE. The highest contribution of the lithospheric mantle to the measured SKS splitting would be achieved for a vertical foliation, which is in agreement with a transpressional deformation in response to the recent convergence between Adria and the European platform. However, the large shear wave splitting delay times measured in the area also imply a significant contribution to seismic anisotropy from the sublithospheric mantle, depending on the depth of the lithosphere-asthenosphere boundary.

Acknowledgments

The authors would like to thank the people who contributed to this work. We owe thanks to Fabrice Barou and David Adams for their help with EBSD-SEM analyses at Geosciences Montpellier and at CCFS Macquarie University, respectively. László Aradi is acknowledged for his help with field work, petrography and MTEX application. We are grateful for the constructive criticism of Sandra Piazolo and Jacques Précigout and two anonymous reviewers, as well as for the editorial handling of Stephen Parman. Our research received financial support from a Marie Curie International Reintegration Grant (grant NAMS-230937), a postdoctoral grant (grant PD101683) of the Hungarian Scientific Research Fund (OTKA), and a Bolyai János Postdoctoral Research Fellowship of the Hungarian Academy of Sciences to I. J. K., as well as from the Lendület Pannon LitH2Oscope Research Group (Research Centre for Astronomy and Earth Sciences, Hungarian Academy of Sciences). N. L. received support from Macquarie University international PhD scholarship and project and travel funding from ARC Centre of Excellence for Core to Crust Fluid Systems (CCFS). K. H. acknowledges funding from Ministry of Economy, Industry and Competitiveness (MINECO, Spain) and the State Research Agency (AEI, Spain; grants FPDI-2013-16253 and CGL2016-81085-R). Instruments used at Macquarie University are funded by DEST Systemic Infrastructure Grants, ARC LIEF, NCRIS/AuScope, industry partners, and Macquarie University. The data used in this paper are listed in the references, tables, and supporting information. The raw EBSD data are available from the corresponding author upon request. This is the 92nd publication of the Lithosphere Fluid Research Lab (LRG), contribution 1361 from the ARC Centre of Excellence for Core to Crust Fluid Systems (www.ccfs.mq.edu.au) and 1320 from the GEMOC Key Centre (www.gemoc.mq.edu.au).

References

Abramson, E. H., Brown, J. M., Slutsky, L. J., & Zaug, J. (1997). The elastic constants of San Carlos olivine to 17 GPa. *Journal of Geophysical Research*, *102*(B6), 12,253–12,263. https://doi.org/10.1029/97JB00682

Aradi, L. E., Hidas, K., Kovács, I. J., Tommasi, A., Klébesz, R., Garrido, C. J., & Szabó, C. (2017). Fluid-enhanced annealing in the subcontinental lithospheric mantle beneath the westernmost margin of the Carpathian-Pannonian extensional basin system. *Tectonics*, *36*, 2987–3011. https://doi.org/10.1002/2017TC004702

Bachmann, F., Hielscher, R., & Schaeben, H. (2010). Texture analysis with MTEX–free and open source software toolbox. *Solid State Phenomena*, *160*, 63–68. https://doi.org/10.4028/www.scientific.net/SSP.160.63

Bada, G., Horváth, F., Dövényi, P., Szafián, P., Windhoffer, G., & Cloetingh, S. (2007). Present-day stress field and tectonic inversion in the Pannonian basin. *Global and Planetary Change*, *58*(1–4), 165–180. http://doi.org/10.1016/j.gloplacha.2007.01.007

Balázs, A., Burov, E., Matenco, L., Vogt, K., Francois, T., & Cloetingh, S. (2017). Symmetry during the syn- and post-rift evolution of extensional back-arc basins: The role of inherited orogenic structures. *Earth and Planetary Science Letters*, *462*, 86–98. https://doi.org/10.1016/j.epsl.2017.01.015

Balogh, K., Árva-Sós, E., & Pécskay, Z. (1986). K/Ar dating of post Sarmatian alkali basaltic rocks in Hungary. *Acta Mineralogie et Petrographie Szeged*, *28*, 75–93.

Baptiste, V., & Tommasi, A. (2014). Petrophysical constraints on the seismic properties of the Kaapvaal craton mantle root. *Solid Earth Discussions*, *5*(2), 963–1005. https://doi.org/10.5194/sed-5-963-2013

Barruol, G., & Mainprice, D. (1993). A quantitative evaluation of the contribution of crustal rocks to the shear-wave splitting of teleseismic SKS waves. *Physics of the Earth and Planetary Interiors*, *78*(3-4), 281–300. https://doi.org/10.1016/0031-9201(93)90161-2

Ben Ismail, W., & Mainprice, D. (1998). An olivine fabric database: An overview of upper mantle fabrics and seismic anisotropy. *Tectonophysics*, *296*(1-2), 145–157. https://doi.org/10.1016/S0040-1951(98)00141-3

Bestmann, M., Piazolo, S., Spiers, C. J., & Prior, D. J. (2005). Microstructural evolution during initial stages of static recovery and recrystallization: New insights from in-situ heating experiments combined with electron backscatter diffraction analysis. *Journal of Structural Geology*, *27*(3), 447–457. https://doi.org/10.1016/j.jsg.2004.10.006

Bielik, M., Alasonati Tašárová, Z., Zeyen, H., Dérerová, J., Afonso, J.-C., & Csicsay, K. (2010). Improved geophysical image of the Carpathian-Pannonian Basin region. *Acta Geodaetica et Geophysica Hungarica*, *45*(3), 284–298. https://doi.org/10.1556/AGeod.45.2010.3.3

Borthwick, V. E., & Piazolo, S. (2010). Post-deformational annealing at the subgrain scale: Temperature dependent behaviour revealed by in-situ heating experiments on deformed single crystal halite. *Journal of Structural Geology*, *32*(7), 982–996. https://doi.org/10.1016/j.jsg.2010.06.006

Brey, G. P., & Köhler, T. (1990). Geothermobarometry in four-phase lherzolites II. New thermobarometers, and practical assessment of existing thermobarometers. *Journal of Petrology*, *31*(6), 1353–1378. https://doi.org/10.1093/petrology/31.6.1353

Bunge, H. J. (1982). *Texture analysis in materials science*. London, UK: Butterworth.

Coltorti, M., Bonadiman, C., Faccini, B., Grégoire, M., O'Reilly, S. Y., & Powell, W. (2007). Amphiboles from suprasubduction and intraplate lithospheric mantle. *Lithos*, *99*(1-2), 68–84. https://doi.org/10.1016/j.lithos.2007.05.009

Coogan, L. A., Jenkin, G. R., & Wilson, R. N. (2002). Constraining the cooling rate of the lower oceanic crust: A new approach applied to the Oman ophiolite. *Earth and Planetary Science Letters*, *199*(1-2), 127–146. https://doi.org/10.1016/S0012-821X(02)00554-X

Csontos, L. (1995). Tertiary tectonic evolution of the Intra-Carpathian area: A review. *Acta Vulcanologica*, *7*(2), 1–13.

Csontos, L., Nagymarosy, A., Horváth, F., & Kovác, M. (1992). Tertiary evolution of the Intra-Carpathian area: A model. *Tectonophysics*, *208*(1-3), 221–241. https://doi.org/10.1016/0040-1951(92)90346-8

Dando, B. D. E., Stuart, G. W., Houseman, G. A., Hegedüs, E., Brückl, E., & Radovanović, S. (2011). Teleseismic tomography of the mantle in the Carpathian–Pannonian region of central Europe. *Geophysical Journal International*, *186*(1), 11–31. https://doi.org/10.1111/j.1365-246X.2011.04998.x

Demouchy, S., Tommasi, A., Barou, F., Mainprice, D., & Cordier, P. (2012). Deformation of olivine in torsion under hydrous conditions. *Physics of the Earth and Planetary Interiors*, *202-203*, 56–70. https://doi.org/10.1016/j.pepi.2012.05.001

Demouchy, S., Tommasi, A., Boffa Ballaran, T., & Cordier, P. (2013). Low strength of Earth's uppermost mantle inferred from tri-axial deformation experiments on dry olivine crystals. *Physics of the Earth and Planetary Interiors*, *220*, 37–49. https://doi.org/10.1016/j.pepi.2013.04.008

Embey-Isztin, A., Downes, H., James, D. E., Upton, B. G. J., Dobosi, G., Ingram, G. A., & Scharbert, R. S. H. H. G. (1993). The petrogenesis of Pliocene alkaline volcanic rocks from the Pannonian Basin, Eastern Central Europe. *Journal of Petrology*, *34*(2), 317–343. https://doi.org/10.1093/petrology/34.2.317

Falus, G., Tommasi, A., Ingrin, J., & Szabó, C. (2008). Deformation and seismic anisotropy of the lithospheric mantle in the southeastern Carpathians inferred from the study of mantle xenoliths. *Earth and Planetary Science Letters*, *272*(1–2), 50–64. https://doi.org/10.1016/j.epsl.2008.04.035

Falus, G., Tommasi, A., & Soustelle, V. (2011). The effect of dynamic recrystallization on olivine crystal preferred orientations in mantle xenoliths deformed under varied stress conditions. *Journal of Structural Geology*, *33*(11), 1528–1540. https://doi.org/10.1016/j.jsg.2011.09.010

Fodor, L., Csontos, L., Bada, G., Györfi, I., & Benkovics, L. (1999). Tertiary tectonic evolution of the Pannonian basin system and neighbouring orogens: A new synthesis of palaeostress data. In B. Durand, L. Jolivet, F. Horvath, & M. Séranne (Eds.), *The Mediterranean Basins: Tertiary Extension within the Alpine Orogen*, *Special Publications*, (Vol. 156, pp. 295–334). London: Geological Society. https://doi.org/10.1144/GSL.SP.1999.156.01.15

Green, H., & Radcliffe, S. (1972). Deformation processes in the upper mantle. In H. C. Heard, I. Y. Borg, N. L. Carter, & C. B. Raleigh (Eds.), *Flow and fracture of rocks*, (pp. 139–156). Washington D. C: American Geophysical Union.

Griffin, W. L., O'Reilly, S. Y., Afonso, J. C., & Begg, G. C. (2009). The composition and evolution of lithospheric mantle: A re-evaluation and its tectonic implications. *Journal of Petrology*, *50*(7), 1185–1204. https://doi.org/10.1093/petrology/egn033

Griffin, W. L., O'Reilly, S. Y., & Ryan, C. (1999). The composition and origin of subcontinental lithospheric mantle. In Y. Fei, C. Bertka, & B. Mysen (Eds.), *Mantle petrology: Field observation and high-pressure experimentation: A tribute to Francis R. (Joe) Boyd*, (pp. 13–45). Houston: The Geochemical Society.

Harangi, S., & Lenkey, L. (2007). Genesis of the Neogene to Quaternary volcanism in the Carpathian-Pannonian region: Role of subduction, extension, and mantle plume. In L. Beccaluva, G. Bianchini, & M. Wilson (Eds.), *Special Paper 418: Cenozoic Volcanism in the Mediterranean Area* (Vol. 418, pp. 67–92). Boulder, Colorado (USA): Geological Society of America Location. https://doi.org/10.1130/2007.2418(04)

Herwegh, M., Linckens, J., Ebert, A., Berger, A., & Brodhag, S. (2011). The role of second phases for controlling microstructural evolution in polymineralic rocks: A review. *Journal of Structural Geology*, *33*(12), 1728–1750. https://doi.org/10.1016/j.jsg.2011.08.011

Hidas, K., Falus, G., Szabó, C., Szabó, P. J., Kovács, I., & Földes, T. (2007). Geodynamic implications of flattened tabular equigranular textured peridotites from the Bakony-Balaton Highland Volcanic Field (Western Hungary). *Journal of Geodynamics*, *43*(4-5), 484–503. https://doi.org/10.1016/j.jog.2006.10.007

Hidas, K., Konc, Z., Garrido, C. J., Tommasi, A., Vauchez, A., Padrón-Navarta, J. A., et al. (2016). Flow in the western Mediterranean shallow mantle: Insights from xenoliths in Pliocene alkali basalts from SE Iberia (eastern Betics, Spain). *Tectonics*, *35*, 2657–2676. https://doi.org/10.1002/2016TC004165

Hielscher, R., & Schaeben, H. (2008). A novel pole figure inversion method: Specification of the MTEX algorithm. *Journal of Applied Crystallography*, *41*(6), 1024–1037. https://doi.org/10.1107/s0021889808030112

Higgie, K., & Tommasi, A. (2012). Feedbacks between deformation and melt distribution in the crust–mantle transition zone of the Oman ophiolite. *Earth and Planetary Science Letters*, *359-360*, 61–72. https://doi.org/10.1016/j.epsl.2012.10.003

Holtzman, B. K., Kohlstedt, D. L., Zimmerman, M. E., Heidelbach, F., Hiraga, T., & Hustoft, J. (2003). Melt segregation and strain partitioning: Implications for seismic anisotropy and mantle flow. *Science*, *301*(5637), 1227–1230. https://doi.org/10.1126/science.1087132

Horváth, F. (1993). Towards a mechanical model for the formation of the Pannonian basin. *Tectonophysics*, *226*(1-4), 333–357. https://doi.org/10.1016/0040-1951(93)90126-5

Horváth, F., Bada, G., Szafián, P., Tari, G., Ádám, A., & Cloetingh, S. (2006). Formation and deformation of the Pannonian Basin: Constraints from observational data. *Geological Society, London, Memoirs*, *32*(1), 191–206. https://doi.org/10.1144/GSL.MEM.2006.032.01.11

Horváth, F., Becker, T., Faccenna, C., & Balázs, A. (2014). Static and dynamic support of the Pannonian basin topography. Paper presented at the EGU General Assembly, Vienna, Austria.

Horváth, F., & Cloetingh, S. (1996). Stress-induced late-stage subsidence anomalies in the Pannonian basin. *Tectonophysics*, *266*(1-4), 287–300. https://doi.org/10.1016/S0040-1951(96)00194-1

Horváth, F., & Faccenna, C. (2011). Central Mediterranean mantle flow system and the formation of the Pannonian Basin. Paper presented at the EGU General Assembly, Vienna, Austria.

Hurai, V., Danišík, M., Huraiová, M., Paquette, J.-L., & Ádám, A. (2013). Combined U/Pb and (U–Th)/He geochronometry of basalt maars in Western Carpathians: Implications for age of intraplate volcanism and origin of zircon metasomatism. *Contributions to Mineralogy and Petrology*, *166*(4), 1235–1251. https://doi.org/10.1007/s00410-013-0922-1

Isaak, D. G., Ohno, I., & Lee, P. C. (2006). The elastic constants of monoclinic single-crystal chrome-diopside to 1,300 K. *Physics and Chemistry of Minerals*, *32*(10), 691–699. https://doi.org/10.1007/s00269-005-0047-9

Jackson, J. M., Sinogeikin, S. V., & Bass, J. D. (2007). Sound velocities and single-crystal elasticity of orthoenstatite to 1073 K at ambient pressure. *Physics of the Earth and Planetary Interiors*, *161*(1–2), 1–12. https://doi.org/10.1016/j.pepi.2006.11.002

Jones, A. P., Smith, J. V., Dawson, J. B., & Hansen, E. C. (1983). Metamorphism, partial melting, and K-metasomatism of garnet-scapolite-kyanite granulite xenoliths from Lashaine, Tanzania. *The Journal of Geology*, *91*(2), 143–165. https://doi.org/10.1086/628753

Jung, H., & Karato, S.-i. (2001). Water-induced fabric transitions in olivine. *Science*, *293*(5534), 1460–1463. https://doi.org/10.1126/science.1062235

Kaczmarek, M.-A., & Tommasi, A. (2011). Anatomy of an extensional shear zone in the mantle, Lanzo massif, Italy. *Geochemistry, Geophysics, Geosystems*, *12*, Q0AG06. https://doi.org/10.1029/2011GC003627

Kázmér, M., & Kovács, S. (1985). Permian-Paleogene paleogeography along the eastern part of the Insubric-Periadriatic lineament system: Evidence for continental escape of the Bakony-Drauzug Unit. *Acta Geologica Hungarica*, *28*(1-2), 71–84.

Klébesz, R., Gráczer, Z., Szanyi, G., Liptai, N., Kovács, I., Patkó, L., et al. (2015). Constraints on the thickness and seismic properties of the lithosphere in an extensional setting (Nógrád-Gömör Volcanic Field, Northern Pannonian Basin). *Acta Geodaetica et Geophysica*, *50*(2), 133–149. https://doi.org/10.1007/s40328-014-0094-0

Kohlstedt, D. L. (2007). Properties of rocks and minerals-constitutive equations, rheological behavior, and viscosity of rocks. In G. Schubert (Ed.), *Treatise on geophysics*, (Vol. 2.14, pp. 389–417). Oxford, UK: Elsevier.

Kourim, F., Vauchez, A., Bodinier, J.-L., Alard, O., & Bendaoud, A. (2015). Subcontinental lithosphere reactivation beneath the Hoggar swell (Algeria): Localized deformation, melt channeling and heat advection. *Tectonophysics*, *650*, 18–33. https://doi.org/10.1016/j.tecto.2014.11.012

Kovács, I., Falus, G., Stuart, G., Hidas, K., Szabó, C., Flower, M. F. J., et al. (2012). Seismic anisotropy and deformation patterns in upper mantle xenoliths from the central Carpathian–Pannonian region: Asthenospheric flow as a driving force for Cenozoic extension and extrusion? *Tectonophysics*, *514-517*, 168–179. https://doi.org/10.1016/j.tecto.2011.10.022

Kovács, I., Kiss, J., Török, K., Király, E., Karátson, D., Fancsik, T., et al. (2018). A new conceptual model for the genesis of Plio-Pleistocene alkaline basalts in the Pannonian Basin. Paper presented at the EGU General Assembly, Vienna, Austria.

Kovács, I., Patkó, L., Falus, G., Aradi, L. E., Szanyi, G., Gráczer, Z., & Szabó, C. (2018). Upper mantle xenoliths as sources of geophysical information: The Perşani Mts. area as a case study. *Acta Geodaetica et Geophysica*, *53*(3), 415–438. https://doi.org/10.1007/s40328-018-0231-2

Kovács, I., & Szabó, C. (2008). Middle Miocene volcanism in the vicinity of the Middle Hungarian zone: Evidence for an inherited enriched mantle source. *Journal of Geodynamics*, *45*(1), 1–17. https://doi.org/10.1016/j.jog.2007.06.002

Liang, Y., Sun, C., & Yao, L. (2013). A REE-in-two-pyroxene thermometer for mafic and ultramafic rocks. *Geochimica et Cosmochimica Acta*, *102*, 246–260. https://doi.org/10.1016/j.gca.2012.10.035

Liptai, N., Jung, H., Park, M., & Szabó, C. (2013). Olivine orientation study on upper mantle xenoliths from Bárna-Nagykő, Nógrád-Gömör Volcanic Field (Northern Pannonian Basin, Hungary). *Bulletin of the Hungarian Geological Society* (in Hungarian with English abstract), *143*, 371–382.

Liptai, N., Patkó, L., Kovács, I. J., Hidas, K., Pintér, Z., Jeffries, T., et al. (2017). Multiple metasomatism beneath the Nógrád–Gömör Volcanic Field (Northern Pannonian Basin) revealed by upper mantle peridotite xenoliths. *Journal of Petrology*, *58*(6), 1107–1144. https://doi.org/10.1093/petrology/egx048

Mainprice, D. (1990). A FORTRAN program to calculate seismic anisotropy from the lattice preferred orientation of minerals. *Computers & Geosciences*, *16*(3), 385–393. https://doi.org/10.1016/0098-3004(90)90072-2

Mainprice, D., Bachmann, F., Hielscher, R., & Schaeben, H. (2014). Descriptive tools for the analysis of texture projects with large datasets using MTEX: Strength, symmetry and components. *Geological Society, London, Special Publications*, *409*(1), 251–271. https://doi.org/10.1144/sp409.8

Mainprice, D., Tommasi, A., Couvy, H., Cordier, P., & Frost, D. J. (2005). Pressure sensitivity of olivine slip systems and seismic anisotropy of Earth's upper mantle. *Nature*, *433*(7027), 731–733. https://doi.org/10.1038/nature03266

Márton, E. (1987). Palaeomagnetism and tectonics in the Mediterranean region. *Journal of Geodynamics*, *7*(1-2), 33–57. https://doi.org/10.1016/0264-3707(87)90062-7

Mercier, J. C., & Nicolas, A. (1975). Textures and fabrics of upper-mantle peridotites as illustrated by xenoliths from basalts. *Journal of Petrology*, *16*(1), 454–487. https://doi.org/10.1093/petrology/16.1.454

Mercier, J.-C. C. (1977). Natural peridotites: Chemical and rheological heterogeneity of the upper mantle. (PhD), State University of New York, Stony Brook, NY.

Nimis, P., & Grütter, H. (2010). Internally consistent geothermometers for garnet peridotites and pyroxenites. *Contributions to Mineralogy and Petrology*, *159*(3), 411–427. https://doi.org/10.1007/s00410-009-0455-9

Novák, A., Klébesz, R., Szabó, C., Wesztergom, V., Patkó, L., Liptai, N., et al. (2014). Combined geophysical (magnetotellurics) and geochemical results for determination of the Lithosphere-Asthenosphere Boundary (LAB) beneath the Nógrád-Gömör Volcanic Field. Paper presented at the 22nd EM Induction Workshop, Weimar, Germany.

Patkó, L., Aradi, L., Liptai, N., Bodnar, R., Fedele, L., Kovács, Z., et al. (2013). Wehrlitization processes within the upper mantle beneath the Northern Pannonian Basin (Hungary). Paper presented at the 23rd V. M. Goldschmidt Conference, Florence, Italy.

Patkó, L., Liptai, N., Kovács, I. J., Aradi, L. E., Xia, Q. K., Ingrin, J., et al. (2019). Extremely low structural hydroxyl contents in upper mantle xenoliths from the Nógrád-Gömör Volcanic Field (northern Pannonian Basin): Geodynamic implications and the role of post-eruptive re-equilibration. *Chemical Geology*, *507*, 23–41. https://doi.org/10.1016/j.chemgeo.2018.12.017

Pécskay, Z., Lexa, J., Szakács, A., Balogh, K., Seghedi, I., Konečny, V., et al. (1995). Space and time distribution of Neogene-Quartenary volcanism in the Carpatho-Pannonian Region. *Acta Vulcanologica*, *7*(2), 15–28.

Pécskay, Z., Lexa, J., Szakács, A., Seghedi, I., Balogh, K., Konečny, V., et al. (2006). Geochronology of Neogene magmatism in the Carpathian arc and intra-Carpathian area. *Geologica Carpathica*, *57*, 511–530.

Précigout, J., & Hirth, G. (2014). B-type olivine fabric induced by grain boundary sliding. *Earth and Planetary Science Letters*, *395*, 231–240. https://doi.org/10.1016/j.epsl.2014.03.052

Qorbani, E., Bokelmann, G., Kovács, I., Horváth, F., & Falus, G. (2016). Deformation in the asthenospheric mantle beneath the Carpathian-Pannonian Region. *Journal of Geophysical Research: Solid Earth*, *121*, 6644–6657. https://doi.org/10.1002/2015JB012604

Rampone, E., Vissers, R. L. M., Poggio, M., Scambelluri, M., & Zanetti, A. (2010). Melt migration and intrusion during exhumation of the Alboran lithosphere: The Tallante mantle xenolith record (Betic Cordillera, SE Spain). *Journal of Petrology*, *51*(1-2), 295–325. https://doi.org/10.1093/petrology/egp061

Seghedi, I., & Downes, H. (2011). Geochemistry and tectonic development of Cenozoic magmatism in the Carpathian–Pannonian region. *Gondwana Research*, *20*(4), 655–672. https://doi.org/10.1016/j.gr.2011.06.009

Soustelle, V., Tommasi, A., Demouchy, S., & Franz, L. (2013). Melt-rock interactions, deformation, hydration and seismic properties in the sub-arc lithospheric mantle inferred from xenoliths from seamounts near Lihir, Papua New Guinea. *Tectonophysics*, *608*, 330–345. https://doi.org/10.1016/j.tecto.2013.09.024

Soustelle, V., Tommasi, A., Demouchy, S., & Ionov, D. (2010). Deformation and fluid–rock interaction in the supra-subduction mantle: microstructures and water contents in peridotite xenoliths from the Avacha Volcano, Kamchatka. *Journal of Petrology*, *51*(1-2), 363–394. https://doi.org/10.1093/petrology/egp085

Stegena, L., Géczy, B., & Horváth, F. (1975). Late Cenozoic evolution of the Pannonian basin. *Tectonophysics*, *26*(1-2), 71–90. https://doi.org/10.1016/0040-1951(75)90114-6

Stuart, G., Houseman, G., Dando, B., Hegedus, E., Brueckl, E., Radovanovic, S., et al. (2007). Understanding extension within a convergent orogen: Initial results from the Carpathian Basins Seismic Project. Paper presented at the AGU Fall Meeting, San Francisco, CA.

Szabó, C., & Bodnar, R. (1996). Changing magma ascent rates in the Nógrád-Gömör Volcanic Field Northern Hungary/Southern Slovakia: Evidence from CO_2-rich fluid inclusions in metasomatized upper mantle xenoliths. *Petrology*, *4*, 221–230.

Szabó, C., Falus, G., Zajacz, Z., Kovács, I., & Bali, E. (2004). Composition and evolution of lithosphere beneath the Carpathian–Pannonian Region: a review. *Tectonophysics*, *393*, 119–137. https://doi.org/10.1016/j.tecto.2004.07.031

Szabó, C., Harangi, S., & Csontos, L. (1992). Review of Neogene and Quaternary volcanism of the Carpathian-Pannonian region. *Tectonophysics*, *208*(1-3), 243–256. https://doi.org/10.1016/0040-1951(92)90347-9

Szabó, C., & Taylor, L. A. (1994). Mantle petrology and geochemistry beneath the Nógrád-Gömör Volcanic Field, Carpathian-Pannonian Region. *International Geology Review*, *36*(4), 328–358. https://doi.org/10.1080/00206819409465465

Tašárová, A., Afonso, J. C., Bielik, M., Götze, H. J., & Hók, J. (2009). The lithospheric structure of the Western Carpathian–Pannonian Basin region based on the CELEBRATION 2000 seismic experiment and gravity modelling. *Tectonophysics*, *475*(3–4), 454–469. https://doi.org/10.1016/j.tecto.2009.06.003

Tommasi, A., Mainprice, D., Canova, G., & Chastel, Y. (2000). Viscoplastic self-consistent and equilibrium-based modeling of olivine lattice preferred orientations: Implications for the upper mantle seismic anisotropy. *Journal of Geophysical Research*, *105*(B4), 7893–7908. https://doi.org/10.1029/1999JB900411

Tommasi, A., Tikoff, B., & Vauchez, A. (1999). Upper mantle tectonics: Three-dimensional deformation, olivine crystallographic fabrics and seismic properties. *Earth and Planetary Science Letters*, *168*(1-2), 173–186. https://doi.org/10.1016/S0012-821X(99)00046-1

Tommasi, A., & Vauchez, A. (2015). Heterogeneity and anisotropy in the lithospheric mantle. *Tectonophysics*, *661*, 11–37. https://doi.org/10.1016/j.tecto.2015.07.026

Tommasi, A., Vauchez, A., Godard, M., & Belley, F. (2006). Deformation and melt transport in a highly depleted peridotite massif from the Canadian Cordillera: Implications to seismic anisotropy above subduction zones. *Earth and Planetary Science Letters*, *252*(3-4), 245–259. https://doi.org/10.1016/j.epsl.2006.09.042

Tommasi, A., Vauchez, A., & Ionov, D. A. (2008). Deformation, static recrystallization, and reactive melt transport in shallow subcontinental mantle xenoliths (Tok Cenozoic volcanic field, SE Siberia). *Earth and Planetary Science Letters*, *272*(1–2), 65–77. https://doi.org/10.1016/j.epsl.2008.04.020

Trepmann, C. A., Renner, J., & Druiventak, A. (2013). Experimental deformation and recrystallization of olivine—Processes and timescales of damage healing during postseismic relaxation at mantle depths. *Solid Earth*, *4*(2), 423–450. https://doi.org/10.5194/se-4-423-2013

Van Orman, J. A., Grove, T. L., & Shimizu, N. (2001). Rare earth element diffusion in diopside: Influence of temperature, pressure, and ionic radius, and an elastic model for diffusion in silicates. *Contributions to Mineralogy and Petrology*, *141*(6), 687–703. https://doi.org/10.1007/s004100100269

Vaselli, O., Downes, H., Thirlwall, M. F., Dobosi, G., Coradossi, N., Seghedi, I., et al. (1995). Ultramafic xenoliths in Plio-Pleistocene alkali basalts from the eastern Transylvanian Basin: Depleted mantle enriched by vein metasomatism. *Journal of Petrology*, *36*(1), 23–53. https://doi.org/10.1093/petrology/36.1.23

Vaselli, O., Downes, H., Thirlwall, M. F., Vannucci, R., & Coradossi, N. (1996). Spinel-peridotite xenoliths from Kapfenstein (Graz Basin, Eastern Austria): A geochemical and petrological study. *Mineralogy and Petrology*, *57*(1-2), 23–50. https://doi.org/10.1007/BF01161620

Vauchez, A., Dineur, F., & Rudnick, R. (2005). Microstructure, texture and seismic anisotropy of the lithospheric mantle above a mantle plume: Insights from the Labait volcano xenoliths (Tanzania). *Earth and Planetary Science Letters*, *232*(3-4), 295–314. https://doi.org/10.1016/j.epsl.2005.01.024

Vauchez, A., & Garrido, C. J. (2001). Seismic properties of an asthenospherized lithospheric mantle: Constraints from lattice preferred orientations in peridotite from the Ronda massif. *Earth and Planetary Science Letters*, *192*(2), 235–249. https://doi.org/10.1016/S0012-821X(01)00448-4

Vauchez, A., Tommasi, A., & Mainprice, D. (2012). Faults (shear zones) in the Earth's mantle. *Tectonophysics*, *558-559*, 1–27. https://doi.org/10.1016/j.tecto.2012.06.006

Waff, H. S., & Faul, U. H. (1992). Effects of crystalline anisotropy on fluid distribution in ultramafic partial melts. *Journal of Geophysical Research*, *97*(B6), 9003–9014. https://doi.org/10.1029/92JB00066

Wright, S. I., Nowell, M. M., & Field, D. P. (2011). A review of strain analysis using electron backscatter diffraction. *Microscopy and Microanalysis*, *17*(3), 316–329. https://doi.org/10.1017/S1431927611000055

Zaffarana, C., Tommasi, A., Vauchez, A., & Grégoire, M. (2014). Microstructures and seismic properties of south Patagonian mantle xenoliths (Gobernador Gregores and Pali Aike). *Tectonophysics*, *621*, 175–197. https://doi.org/10.1016/j.tecto.2014.02.017

References From the Supporting Information

Vollmer, F. W. (1990). An application of eigenvalue methods to structural domain analysis. *Geological Society of America Bulletin*, *102*(6), 786–791. https://doi.org/10.1130/0016-7606(1990)102<0786:AAOEMT>2.3.CO;2